



## OPEN ACCESS

## EDITED BY

Dongming Zhi,  
PetroChina, China

## REVIEWED BY

Zhanfeng Qiao,  
PetroChina Hangzhou Research  
Institute of Geology, China  
Xiucheng Tan,  
Southwest Petroleum University, China  
Yuefeng Shen,  
Hefei University of Technology, China

## \*CORRESPONDENCE

Youli Wan,  
wanyouli@cdut.edu.cn  
Jiashan Lin,  
sumlin\_2021@163.com

## SPECIALTY SECTION

This article was submitted to Economic  
Geology,  
a section of the journal  
Frontiers in Earth Science

RECEIVED 15 May 2022

ACCEPTED 11 July 2022

PUBLISHED 25 August 2022

## CITATION

Wan Y, Lin J, Zhao Z and Wang Z (2022),  
Origin of the dolomite in the Buqu  
Formation (Mid-Jurassic) in the south  
depression of the Qiangtang Basin,  
Tibet: Evidence from petrographic and  
geochemical constraints.  
*Front. Earth Sci.* 10:944701.  
doi: 10.3389/feart.2022.944701

## COPYRIGHT

© 2022 Wan, Lin, Zhao and Wang. This is  
an open-access article distributed  
under the terms of the [Creative  
Commons Attribution License \(CC BY\)](https://creativecommons.org/licenses/by/4.0/).  
The use, distribution or reproduction in  
other forums is permitted, provided the  
original author(s) and the copyright  
owner(s) are credited and that the  
original publication in this journal is  
cited, in accordance with accepted  
academic practice. No use, distribution  
or reproduction is permitted which does  
not comply with these terms.

# Origin of the dolomite in the Buqu Formation (Mid-Jurassic) in the south depression of the Qiangtang Basin, Tibet: Evidence from petrographic and geochemical constraints

Youli Wan<sup>1,2\*</sup>, Jiashan Lin<sup>1,2\*</sup>, Zhan Zhao<sup>1,2</sup> and  
Zhonglin Wang<sup>1,3</sup>

<sup>1</sup>Key Laboratory of Sedimentary Basin and Oil and Gas Resources, Ministry of Natural and Resources, Chengdu, China, <sup>2</sup>Chengdu Center, China Geological Survey, Chengdu, China, <sup>3</sup>College of Earth Sciences, Chengdu University of Technology, Chengdu, China

The Qiangtang Mesozoic sedimentary basin is a new field of hydrocarbon exploration, in which the Buqu Formation dolostone reservoirs have attracted increasing attention in recent years. To determine the origin of these reservoirs, petrographic study, fluid inclusion thermometry dating, and C-O and Sr isotopic dating were performed. The results revealed the genesis and evolution of different types of dolomite matrix and cement, as follows: 1) The dolomite texture in the study area is closely related to its formation environment and process and can be categorized as primary fabric well-preserved dolomite (Rd1), primary fabric poorly-preserved dolomite, and dolomite filling. The primary fabric-poorly-preserved dolomite includes fine-grained euhedral dolomite (Rd2), fine-grained planar subhedral dolomite (Rd3), and medium-to coarse-grained anhedral dolomite (Rd4). The dolomite filling includes fine-grained planar subhedral cave-filling dolomite (Cd1) and medium-to coarse-grained anhedral, saddle dolomite (Cd2). 2) Rd1 has  $\delta^{13}\text{C}_{\text{‰PDB}}$  of 3.42‰–4.23‰,  $\delta^{18}\text{O}_{\text{‰PDB}}$  from –4.22‰ to –3.37‰, and  $^{87}\text{Sr}/^{86}\text{Sr}$  of 0.707654–0.708176 and was formed in the contemporaneous or penecontemporaneous stage at low temperatures by mimic replacement related to seawater evaporation. Abundant supersaturated dolomitization fluids favored the preservation of its primary dolomite texture. 3) Rd2 has  $\delta^{13}\text{C}_{\text{‰PDB}}$  of 3.18‰–4.11‰,  $\delta^{18}\text{O}_{\text{‰PDB}}$  from –4.56‰ to –4.23‰, and  $^{87}\text{Sr}/^{86}\text{Sr}$  (0.707525–0.708037), while Rd3 has  $\delta^{13}\text{C}_{\text{‰PDB}}$  of 2.72‰–4.42‰,  $\delta^{18}\text{O}_{\text{‰PDB}}$  from –6.57‰ to –5.56‰, and  $^{87}\text{Sr}/^{86}\text{Sr}$  of 0.707432–0.707990. Both were formed at low temperatures in the shallow-burial stage, when the dolomitization fluid was mainly derived from seawater. Excessive dolomitization during the late shallow-burial stage caused the destruction of the dolomite crystals from euhedral to subhedral. 4) Rd4 has  $\delta^{13}\text{C}_{\text{‰PDB}}$  of 3.24‰–4.14‰,  $\delta^{18}\text{O}_{\text{‰PDB}}$  from –8.22‰ to –6.37‰, and  $^{87}\text{Sr}/^{86}\text{Sr}$  of 0.707234–0.707884 and resulted from dolomitization or recrystallization at high temperatures in the medium-to deep-burial stage. The crystal curvature

was caused by high environmental temperatures. Cd1 has  $\delta^{13}\text{C}_{\text{PDB}}$  of 3.02‰,  $\delta^{18}\text{O}_{\text{PDB}}$  of -5.13‰, and  $^{87}\text{Sr}/^{86}\text{Sr}$  of 0.708147 and was formed during cavern filling before the shallow-burial stage. Cd2 has  $\delta^{13}\text{C}_{\text{PDB}}$  of -0.09‰–3.38‰,  $\delta^{18}\text{O}_{\text{PDB}}$  from -10.41‰ to -8.56‰, and  $^{87}\text{Sr}/^{86}\text{Sr}$  of 0.708180–0.708876 and was related to the collisional orogeny between the Lhasa terrane and the Qiangtang Basin in the late Early Cretaceous. Fluids in the overlying and underlying clastic strata of the Buqu Formation were driven by the thermal hot spot during compressional tectonic setting. These fluids caused negative shifts in the oxygen isotope compositions of the earlier dolomite.

#### KEYWORDS

dolomitization, dolomite texture, geochemistry, Buqu Formation, Qiangtang basin

## 1 Introduction

Dolostone reservoirs are an important target for carbonate oil and gas exploration (Dai et al., 2020; Fu et al., 2021; Liu et al., 2021; Yang et al., 2021; Yue et al., 2021). In 1791, French geologist Déodat de Dolomieu discovered and named the dolomite mineral in the Dolomieu mountain in Italy. For more than two centuries, the “dolomite problem” has challenged geologists and oil explorers. The complexity of dolomite has made it difficult to determine its origin, which has become a core topic of debate (Huang et al., 2021). Hence, based on petrographic and geochemical data, researchers worldwide have reported on the driving mechanisms of dolomitization fluid, favorable dolomitization environments, and corresponding macro-level dolomitization models, including the sabkha (McKenzie et al., 1980; Patterson and Kinsman, 1982; Mutti and Simo, 1994), mixed water (Hanshaw et al., 1971; Badiozamani, 1973; Choquette and Steinen, 1980), microbial (organic) (Vasconcelos and McKenzie, 1997), reflux (Adams and Rhodes, 1960; Jones et al., 2003), seawater dolomitization (Purser et al., 1994; Gregg et al., 2001), burial dolomitization (Land, 1985; Morrow, 1998; Mountjoy et al., 1999), and tectonic hydrothermal dolomitization (Qing and Mountjoy, 1994; Lonnee and Machel, 2004; L'opez-Horgue et al., 2010) models, among others. These findings have improved our understanding of dolomite origin and the mechanisms by which dolostone reservoirs are formed. Compared to these macro-scale aspects, little consideration has been given to the genetic implication of dolomite textures, which may be attributed to inadequate textural descriptions (Huang et al., 2011). However, dolomite textures may preserve unique information on the environment, crystallization, crystal growth, and fluid during the formation process, which can be used to study the formation environments and mechanisms (Friedman, 1965; Gregg and Sibley, 1984; Sibley and Gregg, 1987; Huang Q Y. et al., 2014; Lu et al., 2020; Huang et al., 2020; Qiao et al., 2021b; Xiong et al., 2021).

Friedman (1965) was the first to describe the significance of dolomite crystal textures. Using the classification terminology for

migmatite and metamorphic rocks, he divided dolomites into three basic textures: euhedral, subhedral, and anhedral. Based on dolomite synthetic experiments, Gregg and Sibley (1984) and Sibley and Gregg (1987) combined the kinetic theory of crystal growth to propose a more detailed classification scheme based on the crystal size distributions, shapes, and boundary features. First, dolomites were divided into unimodal and multimodal types based on the size distributions of their crystals. They were then divided into planar euhedral (planar-e), planar subhedral (planar-s), and nonplanar anhedral (nonplanar-a) based on their boundary shapes and crystal features. The planar type refers to a straight crystal boundary, whereas the nonplanar/curved type refers to the bent, terraced, or other irregular crystal boundaries. Planar and nonplanar dolomites can exist in the form of cement. This classification scheme defines the critical temperature for crystal transformation from planar type to nonplanar type; namely, the critical temperature of anhedral crystal growth (around 50–60°C). Planar-e or planar-s dolomite is formed below this critical temperature, whereas nonplanar-a dolomite is formed above this critical temperature. Huang S. et al. (2014) assumed a maximum critical temperature of 73°C. Wright (2001) also defined a transition type from planar-s to nonplanar-a, which was supplementary to the scheme proposed by Gregg and Sibley. This classification scheme is highly valued for its easy use and description with certain significance regarding its origin (Amthor and Friedman, 1991; Warren, 2000; Machel, 2004; Huang Q. Y. et al., 2014). Recently, several scholars have studied the relationship between dolomite texture and origin in China. Based on the morphological characteristics of a single dolomite crystal, Wang et al. (2010) developed a structural-genetic classification for dolomites in the burial stages and investigated the relationship between dolomite shapes and the forming environment. Huang et al. (2011) studied the Permian–Triassic dolostones in the Sichuan Basin and analyzed the differences between different dolomites and their relationship in the dolomitization process. However, these studies lacked corresponding geochemical data. The structural-genetic concept was not thoroughly introduced until Huang S. et al. (2014) described a structural classification based

on the Cambrian–Ordovician dolostones in the central uplift region of the Tarim Basin combined with C–O–Sr isotope data to investigate the origin of different types of dolomites (Yu et al., 2020).

The Qiangtang Mesozoic Marine sedimentary basin is the least explored oil-bearing basin in China. In recent years, dolostone paleo-reservoirs were discovered in the middle Jurassic Buqu Formation in the southern Qiangtang depression, providing a new direction for oil and gas exploration in the basin (Chen et al., 2018; Wang and Fu, 2018; Sun et al., 2020; Wang et al., 2020; Yi and Xia, 2022). The dolostone reservoir in the Buqu Formation has attracted attention as a high-quality reservoir under the overall dense background of oil and gas reservoirs in the Qiangtang Basin (Tan et al., 2004; Sun et al., 2020; Yi and Xia, 2022). Many researchers have conducted fruitful studies on this reservoir regarding the sedimentary environment, dolomite genesis, reservoir characteristics, etc. However, controversy remains about the dolomite genesis, including the mixed water model (Yi et al., 2004; Zhang et al., 2005; Chen et al., 2006; Liu et al., 2008a, b, c, 2010; Peng et al., 2008), high-temperature formation water (Yi et al., 2014; Li et al., 2018), tectonic hydrothermal fluids (Tian et al., 2019; Ji et al., 2020), burial dolomitization (Sun et al., 2020), and multi-stage dolomitization superimposes (Wan et al., 2017a, b, 2018a, b, 2020, 2021), all of which have restricted the discovery of oil and gas. The core dispute centers on the source and formation environment of dolomitization fluid; namely, whether it is seawater, concentrated brine trapped by strata, or meteoric water. Moreover, questions remain regarding whether the dolomite formed in a shallow-burial low-temperature environment or deep-burial high-temperature environments and if dolomitization occurred under a normal geothermal gradient or abnormal high-temperature hydrothermal condition.

This study investigated the petrography, geochemistry, and origin of various types of dolomites collected from the QZ11, QZ12, and QK-1 wells using various methods, including core description; petrographic observation; cathodoluminescence imaging; and carbon (C), oxygen (O), and strontium (Sr) isotope analyses. Combined with fluid inclusion measurement and salinity analysis, this study aimed to reveal the genetic mechanism of the dolostone in the Buqu Formation and provide a geological basis for the evaluation of the dolostone reservoir.

## 2 Geological setting

The Qiangtang Basin, located in the hinterland of the Qinghai-Tibet Plateau, is a marine sedimentary basin formed in the Mesozoic Era on the pre-Ordovician crystalline basement (Tan et al., 2016). The Qiangtang Basin is bounded by the Kekexili–Jinsha River suture zone (KJS) in the north and the

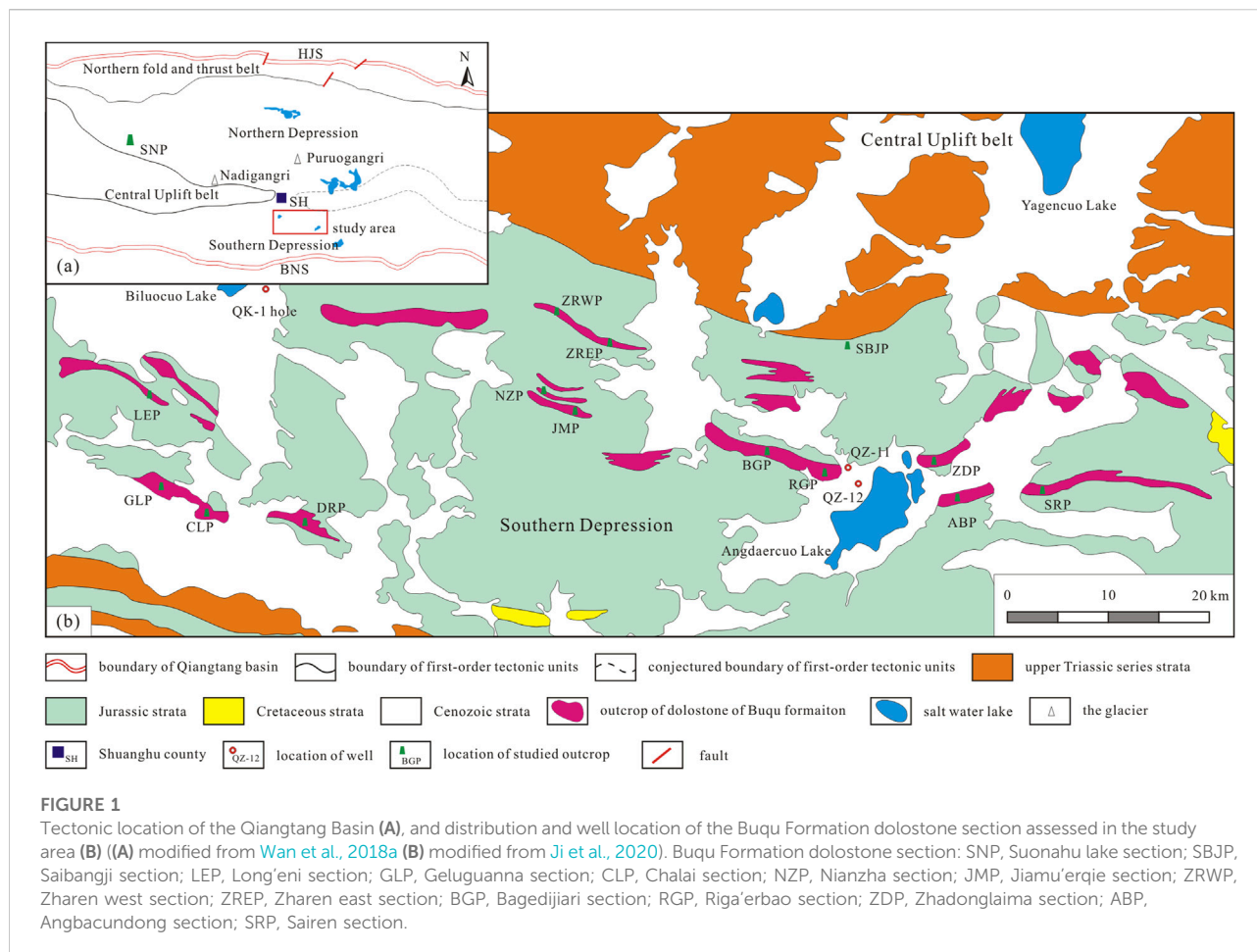
Bangong Lake–Nujiang suture zone (BNS) in the south (Yang et al., 2000). Its structural framework can be divided into four first-order tectonic units: the northern fold and thrust belt, the northern depression belt, the central uplift belt, and the southern depression belt (Wang et al., 2007; Wan et al., 2021). Overall, the basin presents a tectonic pattern of “two depressions interlocked with one uplift”. The study area was located in the southern depression belt (Figure 1A).

In the early Norian Age of the late Triassic Period, the Qiangtang Basin was under tension due to the opening of the Bangong Lake–Nujiang Oceanic Basin in the south. The Southern Qiangtang Depression entered the rift valley stage. Until the late Norian Age–the early Rhaetian Age, the Northern Qiangtang Rift Basin developed, and both the Northern and Southern Qiang Basins simultaneously sank and became sedimentary depressions to form the structural framework in the Qiangtang Basin (Wang et al., 2007). From the early Jurassic Period to the Kimmeridgian Age of the late Jurassic Period, the entire Qiangtang Basin was in a stable uniform environment (Wang et al., 2020). In the Bathonian age of the middle Jurassic Period and the Oxfordian Age–the Kimmeridgian Age of the late Jurassic Period, two large-scale marine transgressions occurred. Seawater submerged the Central Uplift, forming the sedimentary sequence of clastic rocks - carbonate rocks - clastic rocks - carbonate rocks (Table 1).

In the Bathonian Age of the middle Jurassic Period, the first and largest marine transgression occurred in the Qiangtang Basin, which was nearly submerged by seawater. With the reduction in the terrigenous detritus supply, a stable carbonate platform deposition developed in the basin under a hot and arid-semiarid paleoclimate (Pan et al., 2015). Carbonate deposition with a restricted water body developed near the boundary of the open platform in the study area (Chen et al., 2020), which was controlled by the high-frequency relative sea-level change. The underwater plateau in the platform developed into intra-platform beaches and the water body in the intra-beach depression was under salinization in the late high stand systems tract. Due to deposition, the Buqu Formation was impacted by multiple diagenetic fluid media and tectonic movements in the burial-uplift process, forming high-quality reservoirs in the overall tight background of Mesozoic oil and gas reservoirs in the Qiangtang Basin (Wan et al., 2017; Wang et al., 2020). The second stage of the Yanshan Movement and the third stage of the Himalayan Movement had the most significant impacts (Wu et al., 2014, 2016; Ji et al., 2019; Zhao W. Z. et al., 2020).

## 3 Materials and methods

The dolomite samples used in this study were collected from wells QZ11, QZ12, and QK-1 and sections SNP (Figure 1A) and BGP (Figure 1B). We examined 284 thin sections and classified



the textural types of well-preserved fabric, poorly preserved fabric, and texture-destroyed fabric according to classification system proposed by Gregg and Sibley (1984) and Sibley and Gregg (1987), as well as the replacive dolomite and void-filling dolomite cement classification. Fluid inclusion thin sections (33 pieces) of different dolomite texture types were also selected for temperature measurement of the fluid inclusions. Dolomite samples with cavities and fractures filled with high purity and little influence by diagenetic epigenesis (without “misty center and clear rim”) were selected. Micro-sampling was performed with a dental drill (0.05–0.1 mm) to eliminate the influence of filling or transformation by other minerals after dolomitization. A total of three limestone samples and 19 matrix dolomite samples were obtained. Five dolomite filling (cement) and five sparry calcite veins filled with fractures and cavities were used for C-O and Sr isotope analyses. Carbon and oxygen isotope analyses were performed on five granular dolomite samples collected from the SNP sections.

The petrographic and fluid inclusion thin sections were prepared in the State Key Laboratory of Oil and Gas Reservoir Geology and Exploitation of the Chengdu University of Technology.

Thin section identification, cathodoluminescence analysis, scanning electron microscope observation, and fluid inclusion temperature measurement were completed at the Southwest Mineral Resources Supervision and Testing Center, Ministry of Natural Resources. The temperature measurements (homogenization temperature and ice-final melting temperature) of the dolomite fluid inclusions were conducted by LINKAM THMS600 Hot & Cold Stage to measure the misty center and clear rim of the dolomite, respectively.





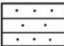

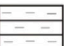
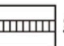


Carbon and oxygen isotope analyses of 27 samples, including limestone, matrix dolomite, and dolomite filling (cement), and Sr isotope analyses of 32 samples were performed at the State Key Laboratory of Oil and Gas Reservoir Geology and Exploitation at the Chengdu University of Technology. The carbon and oxygen isotope analyses were performed on a MAT253, which performed the Sr isotope analyses by thermoelectric ionization solid isotope mass spectrometry (TIMS). Carbon and oxygen isotope analyses of five granular dolomite samples and five sparry calcite veins filled samples were completed by MAT252 isotope mass spectrometry analyzer in the Experimental Testing Center, School of Earth Science and Technology, Southwest Petroleum University. For C-O isotope analyses, pure phosphoric acid was



TABLE 1 Generalized stratigraphic column of the Qiangtang Basin.

System	Series	Stage	Formation		Lithology	
Cretaceous	Lower	?	Northern depression	Sorthern depression		
		Berriasian	Upper Suowa Fm.			
Jurassic	Upper	Tithonian	Lower Suowa Fm.		oolitic limestone	
		Kimmeridgian			limestone	
		Oxfordian				
	Middle	Callovian	Xiali Fm.		sandstone	
		Bathonian	Buqu Fm.		limestone dolomite	
		Bajocian	Qoimaco Fm.	Sewa Fm.	limestone mudstone	
	Lower	Toarcian	Qoimaco Fm.	Quse Fm.		
		?				mudstone
Triassic	Upper	Rhaetian	Nadi Kangri Fm.	?	volcanics	
		Norian	Tumengela Fm.			
		Carnian			sandstone	

	dolomite		oolitic limestone		limestone		muddy limestone		sandstone
	siltstone		mudstone		gypsum		volcanics		unconformity

used to generate CO<sub>2</sub>. The results were presented in δ‰ values as per PDB standards. The test was taken as per DZ/T0184.17–1997, with an analytical error of ±0.0005%. Sr isotope analyses were performed as per the standard Sample NBS987 of the US National Bureau of Standards, with an analytical error of the specific value of <sup>87</sup>Sr/<sup>86</sup>Sr of ±0.002%.

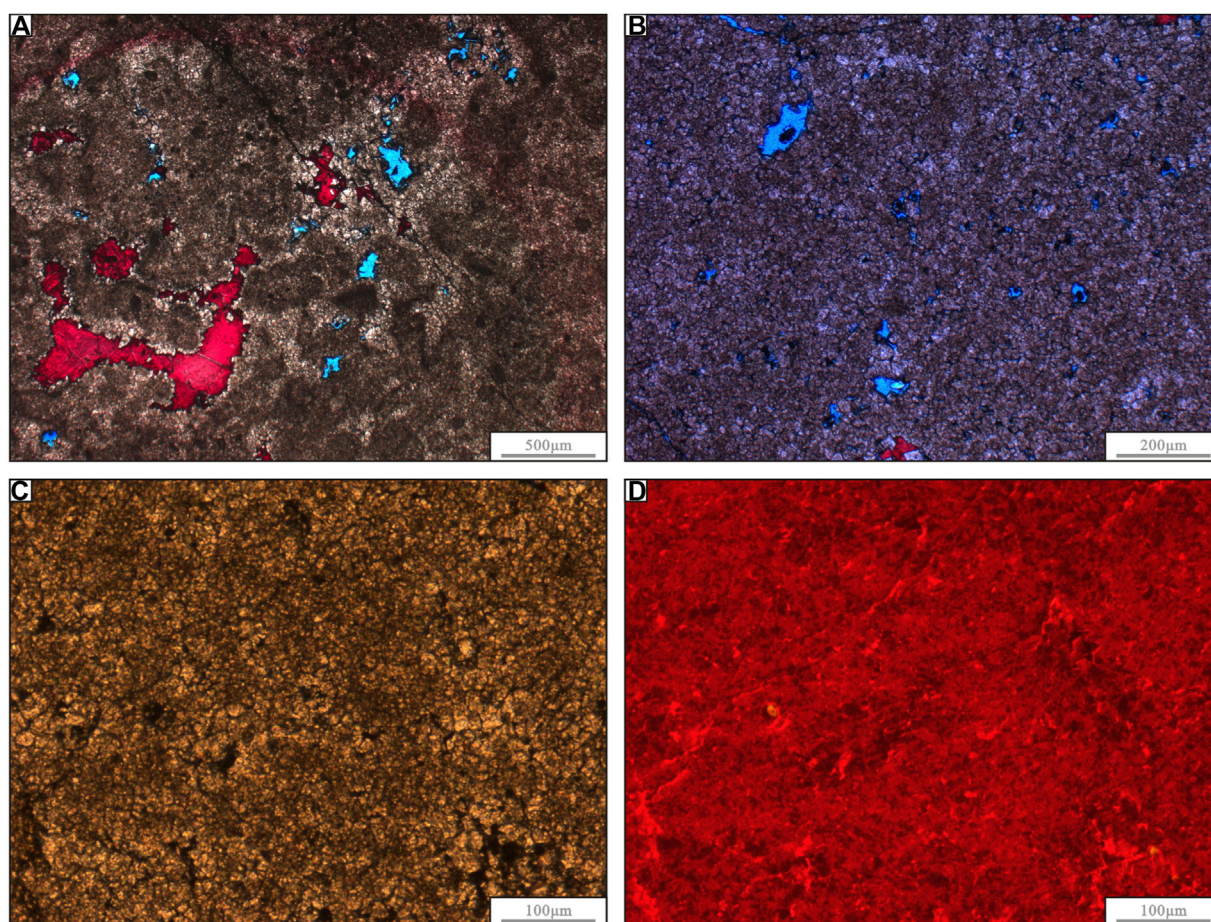
## 4 Petrographic study

According to the profile geological survey data (BGP section) (Figure 1), the dolostone of the Buqu Formation in this study area was mainly fine crystal dolomite (Wan et al., 2017a). Core observation showed that the formation dip angle of the Buqu Formation encountered in well QZ12 was >50°, with enlarged thickness of severely weathered strata. The profile of a single well showed that the dolomite of the Buqu Formation developed at well depths of 213.56–4.25 m, with 81 “limestone-dolomite” meter-level lithologic cycles. In each cycle, thin-bedded “micritic limestone to micritic arenaceous limestone to sparry arenaceous limestone to calcareous dolomite to dolomite (fine-grained dolomite or medium-coarse grained dolomite)” developed from

the bottom to the top, with the thicknesses of each lithologic segment ranging from 40 to 80 cm (Wan et al., 2017a; Wan et al., 2018a; Wan et al., 2020). Under the microscope, the samples from well QZ12 were mainly composed of fine-grained euhedral dolomite and fine-grained subhedral dolomite, followed by medium-coarse-grained dolomite and a small amount of microcrystalline dolomite. Only six of the 154 samples were saddle dolomite. The 600.00–575.00 m section of well QZ11 was pinhole dolomite, with saddle dolomite filling commonly observed. Saddle dolomite was found in half of the 64 samples in the core of the QK-1 hole, with equal fine-grained and medium-coarse-grained dolomite.

Two different varieties of dolomite were identified according to the primary fabric preservation (Huang Q. Y. et al., 2014): fabric-well-preserved dolomite (Rd1) and fabric-poorly preserved or fabric-destructive dolomite. Three different varieties of five different types of dolomite and fabrics were identified according to the crystal size distribution (unimodal or polymodal) and crystal boundary shape (planar or nonplanar) (Sibley and Gregg, 1987).

According to the preservation of the primary fabric, the dolomite was divided into Rd1 and poorly preserved fabric or



**FIGURE 2**

Petrological characteristics of Rd1. (A) Plane-polarized-light image of an Rd1 sample showing nonplanar-a textures in small areas, with some calcite-filled pores. The sample was obtained from well QZ12 in the Buqu Formation at a depth of 140.86 m. (B) Plane-polarized-light image of an Rd1 sample showing nonplanar-a textures in most areas and an algal stromatolitic texture in some areas, with a few calcite-filled pores. The sample was obtained from well QZ12 in the Buqu Formation at a depth of 65.00 m. (C) Plane-polarized-light image of an Rd1 sample containing relatively dense peloids replaced by nonplanar-a dolomite to varying degrees, as well as scattered asphaltenes. The sample was obtained from well QZ12 in the Buqu Formation at a depth of 134.58 m. (D) Cathodoluminescence image of the Rd1 sample in (C). These crystals show a dull-dull orange light, which is brighter along the grain edge. In contrast, the asphaltene shows no luminescence.

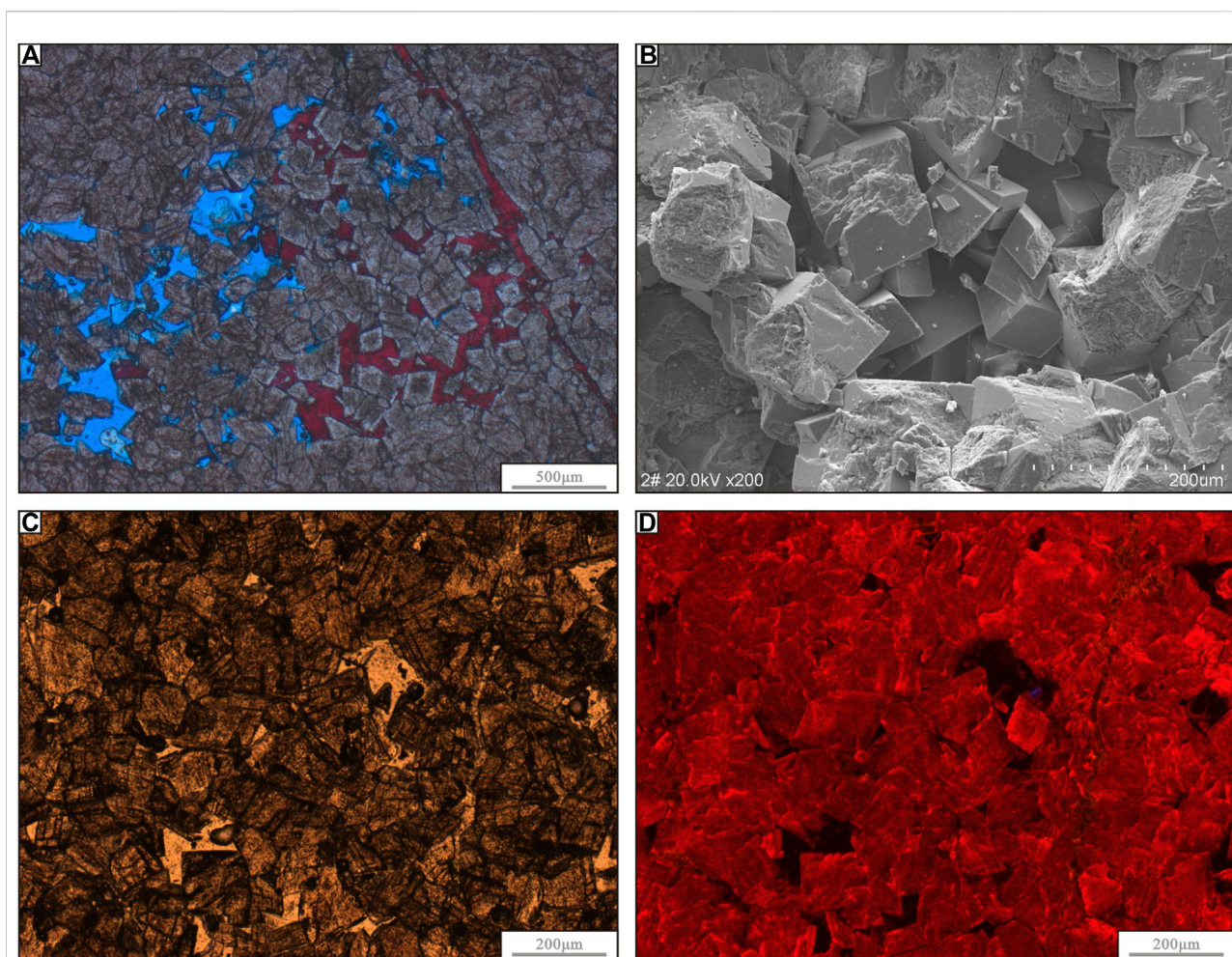
fabric-destructive dolomite (Huang S. et al., 2014). Rd1 preserves primary fabrics well, while poorly preserved fabric or fabric-destructive dolomite is subdivided based on the crystal size and structural features of the dolomite. The crystal textures were classified as proposed by Sibley and Gregg (1987) and adjusted and simplified based on the actual situations in the research area. The crystal textures included euhedral (planar-e crystal), subhedral (mainly planar-s crystal, with some nonplanar-a crystal), and anhedral (nonplanar-a crystal) types. In addition, dolomite can also appear as filling of holes and cracks, which is significant in the analysis of dolomite origin. For instance, saddle-shaped dolomite is often thought to be linked to hydrothermal transformation (Davies and Smith, 2006). Thus, based on dolomite filling (cement), the dolomite of the Buqu Formation in the study area was categorized as Rd1, fine-grained euhedral crystalline dolomite

(Rd2), fine-grained subhedral dolomite (Rd3), medium-to coarse-grained anhedral dolomite (Rd4), and dolomite fillings. The dolomite fillings included fine-grained euhedral-subhedral dolomite (Cd1) and medium-coarse grained saddle-shaped dolomite (Cd2) filling. The preliminary study for this work included an analysis of the trace elements and rare Earth elements for different types of dolomite, which can be mutually verified with this study (Wan et al., 2017b; 2018b).

#### 4.1 Fabric well-preserved dolomite (Rd1)

The fabric-well-preserved dolomite inherits and/or retains the structural characteristics of the precursor limestone, which helps to reconstruct its sedimentary environment.





**FIGURE 3**

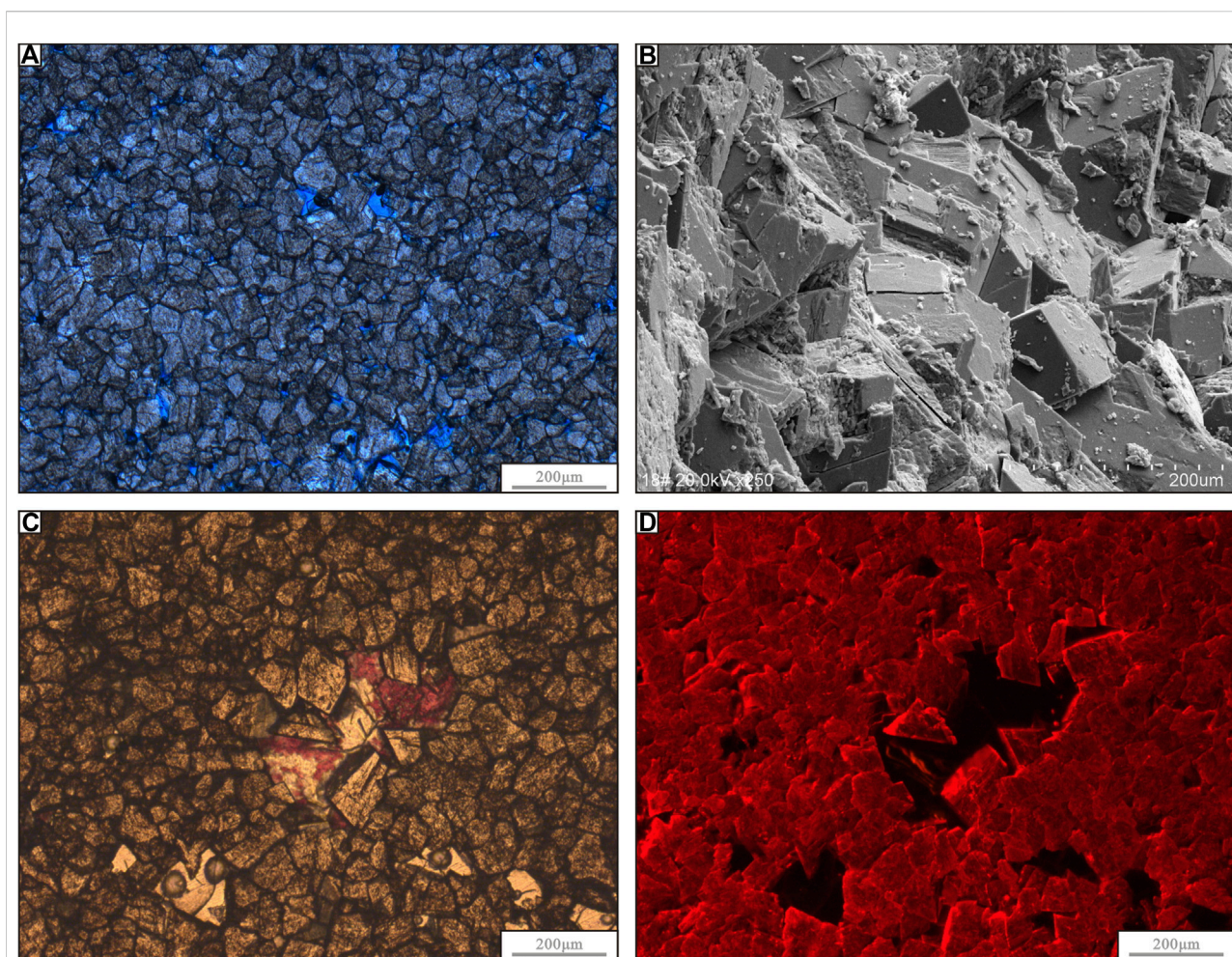
Petrological characteristics of Rd2. (A). Plane-polarized-light image of an Rd2 sample with fine crystalline size and showing planar euhedral textures, some dolomites with misty center and clear rim, and some calcite-filled pores. The sample was obtained from well QK-1 in the Buqu Formation at a depth of 352.74 m. (B). Scanning electron microscope image of an Rd2 sample showing planar euhedral textures, some mostly rhombohedral dolomite, and partially dissolved dolomite. The sample was obtained from well QZ11 in the Buqu Formation at a depth of 597.34 m. (C). Plane-polarized-light image of an Rd2 sample with fine crystalline size showing planar euhedral textures, a few dolomite areas with misty center and clear rim, and unfilled pores. The sample was obtained from well QZ11 in the Buqu Formation at a depth of 581.69 m. (D). Cathodoluminescence image of the Rd2 sample in (C). These crystals show a very dull-dull orange light that is brighter along the crystalline edge. In contrast, the pore shows no luminescence.

Different intensities of metasomatism of the residual structures in the study area lead to different degrees of recognition of precursor limestone particles or plaster (Bi et al., 2001; Yang et al., 2021). The results of the petrographic examination showed fabric-well-preserved dolomite in the study area in the Buqu Formation, which was further divided into two subtypes.

The first subtype of dolomite (Rd1) has intact grain or a stucco outline; some scholars have termed the internal structure “mimic/mimetic replacement” (Kaldi and Gidman, 1982; Sibley, 1991). Combined with the inferred primordia fabric of the precursor limestone, this subtype

contains granular (Figure 2A) and mud-silty (Figures 2B,C) dolomites. The muddy-silty dolomite in the Buqu Formation in the study area mostly retained the primary fabric of the residual precursor limestone, and single muddy-silty dolomite was rarely observed. This type of dolomite mainly consists of muddy-silty dolomite (0.001–0.05 mm) with tiny, mostly subhedral-anhedral, crystals. The other subtype, residual grain dolomite, only retains the shape or outline of the original particles with unrecognizable internal structures. It is rarely observed in the Buqu Formation. Primary Rd1 in this study refers to the mimetic crystal metasomatic dolomite.





**FIGURE 4**

Petrological characteristics of Rd3. **(A)** Plane-polarized-light image of an Rd3 sample with fine crystalline size showing planar subhedral textures, several dolomite areas with misty centers and clear rims, as well as unfilled pores. The sample was obtained from well QK-1 in the Buqu Formation at a depth of 351.94 m. **(B)** Scanning electron microscope image of an Rd3 sample showing planar subhedral textures due to dense dolomite overgrowth. The sample was obtained from well QZ12 in the Buqu Formation at a depth of 105.02 m. **(C)** Plane-polarized-light image of an Rd3 sample with fine crystalline size showing planar subhedral textures, several areas of dolomite with misty centers and clear rims, and some calcite-filled pores. The sample was obtained from well QZ12 in the Buqu Formation at a depth of 54.86 m. **(D)** Cathodoluminescence image of the Rd2 sample in **(C)**. These crystals show a very dull-dull orange, which is brighter in a few dolomite areas along the crystalline edge. The pores and calcite cement show no luminescence.

## 4.2 Fabric poorly preserved or fabric-destructive dolomite

### 4.2.1 Euhedral planar crystalline dolomite (Rd2)

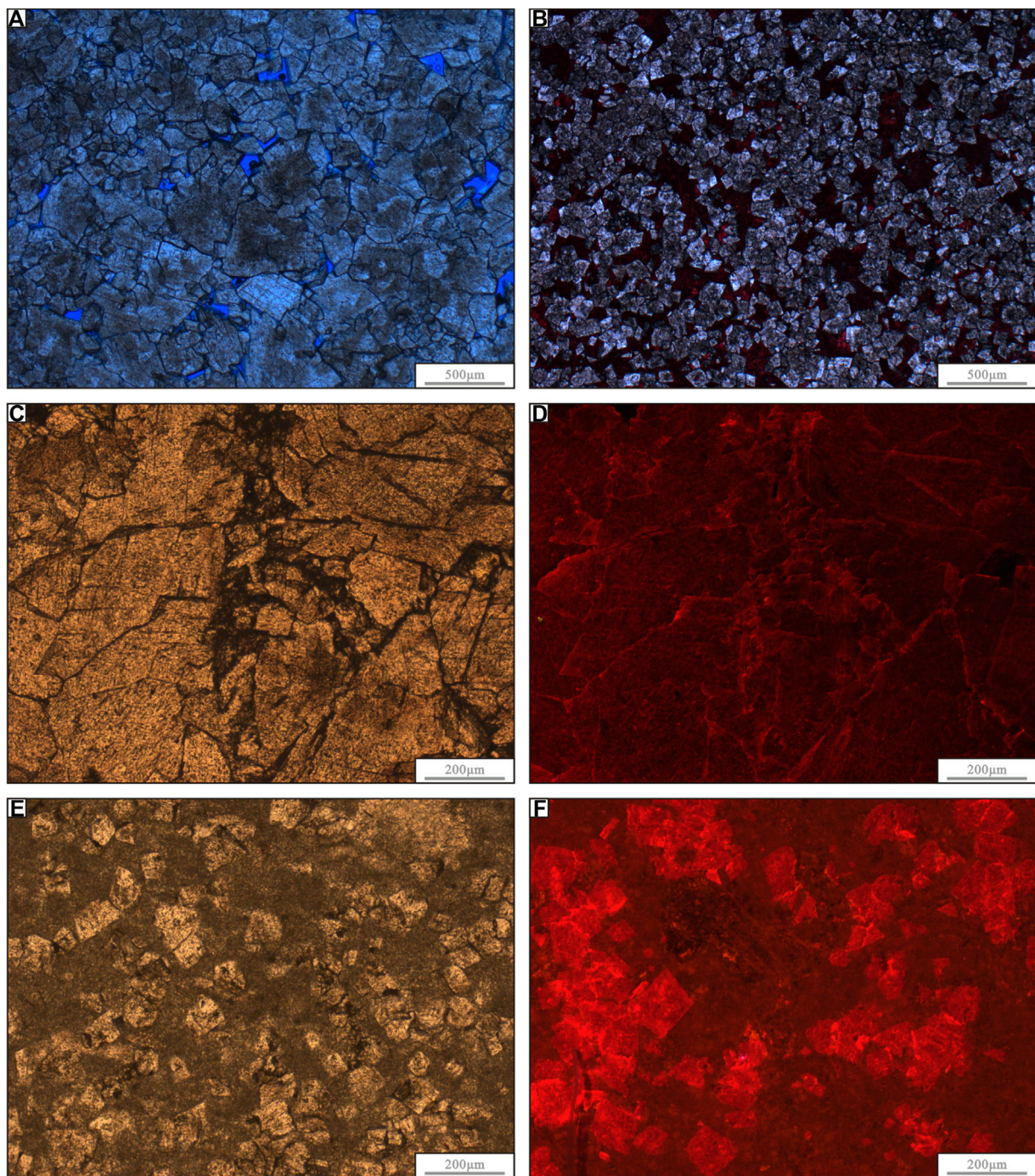
This type of dolomite (Rd2) is also referred to as “sugar” dolostone (Ji et al., 2020). The core sample and field profiles showed light-dark gray, medium to thick layers or lumpy occurrence, with locally visible traces of bioturbation or fossil fragments of shell organisms. Rd2 contained mostly fine grains (0.05–0.25 mm) and a small number of powdered crystals, with a high degree of self-morphism and sugar-like characteristics under a microscope. The crystals were highly euhedral and saccharoidal. Bright fine rings or “misty center

and clear rim” structures were observed at the edge of some crystals (Figure 3A), with intercrystalline point/line contacts and pores. Under scanning electron microscopy, Rd2 was mostly composed of rhombohedral dolomite with flat crystal boundaries (Figure 3B). Cathodoluminescence showed uniform medium brightness and orange to dark red color (Figures 3C,D).

### 4.2.2 Fine-grained subhedral planar crystalline dolomite (Rd3)

In the core sample and the field cross-section, dolomite (Rd3) was mainly dark gray to gray in color and is slightly deeper than or interbedded with the fine crystal and euhedral dolomites. The crystals were mainly fine (0.05–0.25 mm), with minor medium

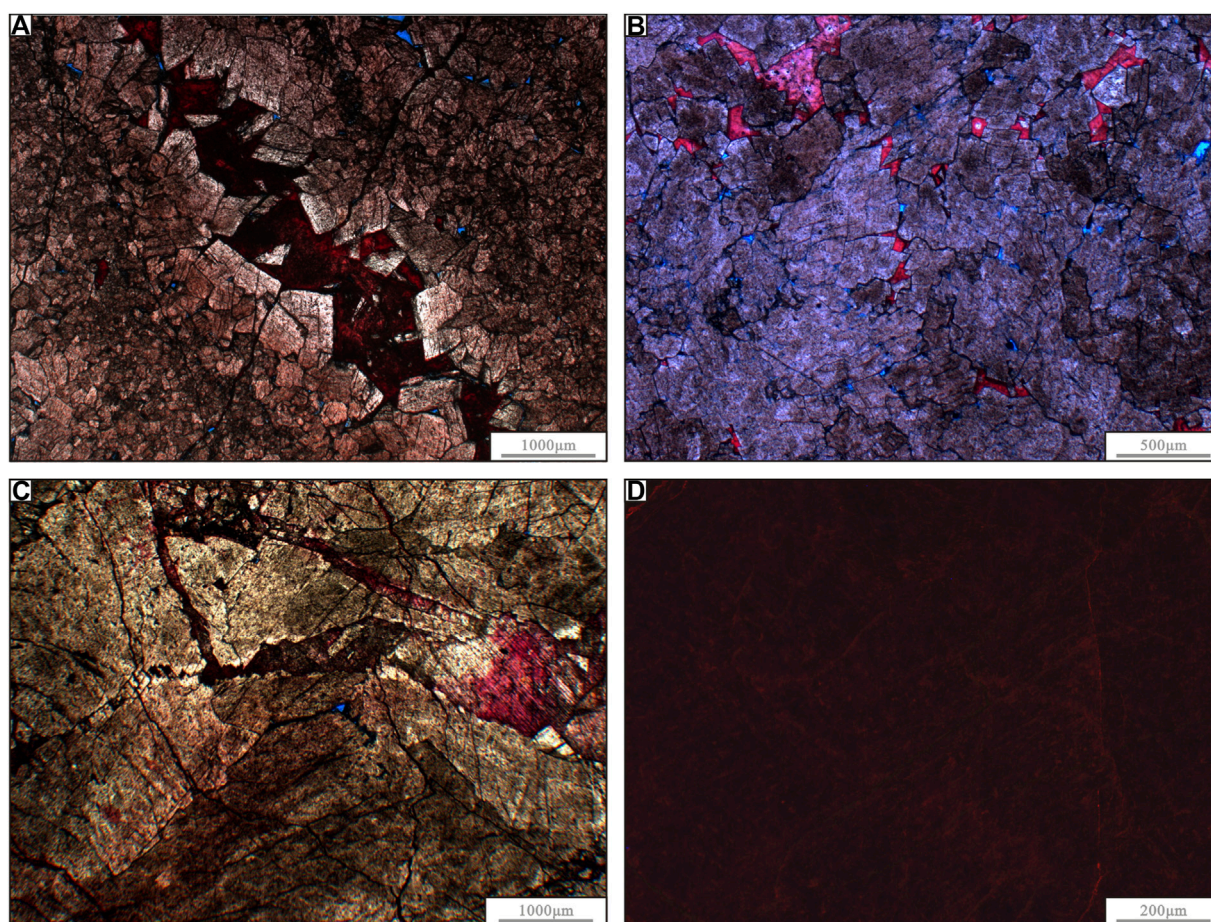




**FIGURE 5**

Petrological characteristics of Rd4. **(A)** Plane-polarized-light image of an Rd4 sample with medium-coarse crystalline size showing anhedral texture, some dolomite with misty centers and clear rims, and unfilled pores. The sample was obtained from well QK-1 in the Buqu Formation at a depth of 308.97 m. **(B)** Plane-polarized-light image of an Rd4 sample showing incomplete dolomitization, and the accumulation of a fine dolomite crystal mosaic. The sample was obtained from well QZ12 in the Buqu Formation at a depth of 105.02 m. **(C)** Plane-polarized-light image of an Rd4 sample with coarse crystalline size showing planar subhedral textures and asphalt-filled microcracks. The sample was obtained from well QZ12 in the Buqu Formation at a depth of 54.86 m. **(D)** Cathodoluminescence image of the Rd4 sample in **(C)**. These crystals show a very dull red, which is brighter in a few dolomite areas along the crystalline edge. **(E)** Plane-polarized-light image of an Rd4 sample showing fine crystal dolomite with incomplete dolomitization. The sample was obtained from well QZ12 in the Buqu Formation at a depth of 66.26 m. **(F)** Cathodoluminescence image of the Rd4 sample in **(E)**. These crystals show a dull red, while the calcite does not emit light.





**FIGURE 6**

Petrological characteristics of void-filling dolomite/dolomite cement. (A). Plane-polarized-light image of a Cd1 sample with fine-medium crystalline size showing dolomite cement filling along the inner wall of the calcite-filled fracture. The sample was obtained from well QZ12 in the Buqu Formation at a depth of 62.75 m. (B). Plane-polarized-light image of a Cd2 sample showing filled saddle dolomite in Rd3. The fractures are well developed and filled with calcite. The sample was obtained from well QZ12 in the Buqu Formation at a depth of 73.38 m. (C). Plane-polarized-light image of a Cd2 sample showing saddle dolomite with calcite-filled fractures. The sample was obtained from well QZ11 in the Buqu Formation at a depth of 580.90 m. (D). Cathodoluminescence image of the Cd2 sample in (C). These crystals show no visible cathodoluminescence.

grains (0.25–0.5 mm) and powder (0.006–0.05 mm). The crystals were mainly subhedral and anhedral and mainly in point or line contact, with some parts in embedded contact. The intercrystalline pores were drastically reduced compared to those in Rd2 (Figure 4A). The dolomite was tightly accumulated in scanning electron microscope examination. Although some crystals showed straight grain boundaries, they were restricted by their growing space. The crystal morphology was incomplete, or they were embedded in neighboring crystals and occupied the original interstitial space. Perfect rhombohedral crystals were observed in the direction toward the intercrystalline pores. (Figure 4B). The cathodoluminescence of such dolomite was predominately dark red in color, similar to or weaker than that of Rd2 (Figures 4C,D).

#### 4.2.3 Medium-to coarse-grained anhedral crystalline dolomite (Rd4)

Rd4 was mainly composed of allomorphic dolomite with a poor degree of crystallography. Medium-/coarse-grained dolomite (0.25–2 mm) was dominant, followed by fine dolomite (0.05–0.25 mm). Rd4 showed two occurrences. One was a transitional type between limestone and dolostone due to incomplete or selective dolomitization. The mottled rock generally developed in the core of well QZ12 (Figures 5B–E), which presented as two-tone punctate, plaque, or ribbon. Microscopic observation showed that the dolomite grain was relatively thin, with mostly fine-medium grains, poor crystal automorphism, and well-developed intergranular pores (Figure 5B). The cathodoluminescence of Rd4 was mainly dark red in color or speckled, with bright orange bands or

TABLE 2 Homogenization and ice-final melting temperatures of fluid inclusions in different dolomites.

Dolomite texture	Occurrence	Homogenization, °C			Ice-final melting temperatures, °C			Salinity,%	Features of fluid inclusions	
		Mean	Maximum	Minimum	Mean	Maximum	Minimum		Number	Degree of development
RD1	Replacive									Very low
RD2-misty left	Replacive	73.24	83	65.5	-17.6	-16.2	-20.1	20.64	5	Low
RD2-clear rim	Recrystal	122.25	123.4	121.1	-20.15	-20	-20.3	22.48	2	Very High
RD3-misty left	Replacive	90.18	98	82.9	-17.05	-13	-19.7	20.21	19	Low
RD3-clear rim	Recrystal	126.75	157	102.8	-17.8	-12.8	-21.1	20.75	22	Very High
RD4-misty left	Replacive	102.67	117	84	-18.15	-13.6	-21.3	21.03	52	High
RD4-clear rim	Recrystal	130.15	145	118	-18.69	-10	-21.5	21.37	37	Very High
CD1	Cements	113.5	116.7	110.2	-20	-19.9	-20.1	22.38	3	High
CD2-misty left	Cements	140.43	165	121	-18.58	-13.3	-20.9	21.34	26	Very High
CD2-clear rim	Recrystal	105.15	119.4	89	-18.19	-14.8	-20.4	21.06	26	High

spots visible at the crystal edges or contacts. The overall cathodoluminescent intensity was slightly higher than that of the non-metasomatized limestone (Figure 5F).

The other occurrence of Rd4 was in gray or dark gray massive medium to thick beds. The fractures and dissolution pores in the upper layers of the core were highly developed, accompanied by saddle dolomite filling. Under the microscope, Rd4 showed fine crystals, with medium, and predominantly coarse grains (Figures 5A–C). Some parts of the samples showed double number distributions, with coarse grains surrounding fine grains, namely between coarse grain dolomite packages or around the fine dolomite crystals, with some individuals differing under the coarse grain dolomite in the orthogonal polarization extinction phenomenon. This indicated the influence of recrystallization. This kind of dolomite crystal is dominated by curved plane boundaries. Rd4 showed entirely dark cathodoluminescence, with local dark red patches (Figure 5D).

### 4.3 Void-filling dolomite/dolomite cement

For the dolostone of the Buqu Formation in the study area, it was difficult to determine whether the dolomite growing around the inwall of a cavern or a crack was generated by cementation or metasomatism. Hence, it was described as “filling” rather than “cement” (Wan et al., 2018a). Although only a small amount of dolomite was present in the dolostone, it played a significant role

in determining the property of the diagenetic fluid and identifying the evolutionary process of the formation and cavern filling. This study revealed two types of dolomite fillings in the dolostone of the Buqu Formation.

Fine planar subhedral crystalline cavern-filling dolomite generally acted as the cavern or crack filling by growing on its in-wall (Cd1). These mostly contained fine grains with little silty grains or medium grains and high euhedral degree (straight boundary) in the direction of the holes (Figure 6A). All crystals were clean with fewer impurities and predominant dark red cathodoluminescence with local glowing rings, similar to those observed Rd3.

In the core, the medium-coarse anhedral saddle dolomite filling (Cd2) was mostly light gray and mainly grew along the inner wall of the fracture or dissolution cavity, forming a shell around or filling the cavity. However, the crystal surface was dirty under plane-polarized light, wherein massive solid or liquid inclusions were seen. Microcracks and cleavages had developed inside the crystals. The grain boundary was bending in a sickle shape. Wavy extinction was obvious under cross-polarized light. The dark red ray was predominant in cathodoluminescence, with no light locally (Figure 6D). The saddle dolomite in the Buqu Formation in the study area was in abrupt contact with the surrounding rock, with matrix dolomite filling material (Figure 6B), indicating that the saddle dolomite was formed after matrix dolomite due to late reconstruction.

TABLE 3 C- O and Sr isotope data for the different carbonate rocks in the Buqu Formation.

Sample ID	Sample position	Rock type	$\delta^{13}\text{C}\text{‰}_{\text{PDB}}$	$\delta^{18}\text{O}\text{‰}_{\text{PDB}}$	$^{87}\text{Sr}/^{86}\text{Sr}$	Remarks
YP-33	Yanshiping area	micrite limestone	2.10	-7.40		Tan et al. (2004)
YP-34	Yanshiping area	micrite limestone	2.60	-6.40		Tan et al. (2004)
YP-37-1	Yanshiping area	micrite limestone	2.30	-6.30		Tan et al. (2004)
YP-37-2	Yanshiping area	shell limestone	0.90	-10.20		Tan et al. (2004)
3	Yichangma area	bioclast-bearing	0.86	-12.05		Zhang et al. (2006)
4	Yichangma area	micrite limestone	1.24	-9.70		Zhang et al. (2006)
9	Yichangma area		2.52	-4.02		Zhang et al. (2006)
5	Yichangma area	micrite limestone	1.16	-10.28		Zhang et al. (2006)
6	Yichangma area	micrite limestone	1.79	-7.06		Zhang et al. (2006)
7	Yichangma area	micrite limestone	1.33	-6.24		Zhang et al. (2006)
8	Yichangma area	micrite limestone	2.49	-3.79		Zhang et al. (2006)
22	Yichangma area	micrite limestone	1.41	-10.24		Zhang et al. (2006)
GP32-B1	this study area	bioclast limestone	1.84	-9.04		Ji et al. (2020)
5	this study area	micrite limestone	2.30	-10.30		Ji et al. (2020)
16	this study area	micrite limestone	1.80	-10.90		Ji et al. (2020)
26	this study area	micrite limestone	2.70	-9.90		Ji et al. (2020)
34	this study area	micrite limestone	3.00	-10.50		Ji et al. (2020)
54	this study area	micrite limestone	2.50	-11.90		Ji et al. (2020)
55	this study area	micrite limestone	2.50	-10.50		Ji et al. (2020)
57	this study area	micrite limestone	2.00	-9.10		Ji et al. (2020)
59	this study area	micrite limestone	2.30	-10.20		Ji et al. (2020)
BD30-2	this study area	micrite limestone	0.89	-13.02		Ji et al. (2020)
P9-B1	this study area	micrite limestone	0.46	-11.86		Ji et al. (2020)
P6-B1	this study area	sparry arenaceous limestone	2.06	-11.99		Ji et al. (2020)
P15-B2	this study area	sparry arenaceous limestone	1.71	-9.68		Ji et al. (2020)
BD16-B4	this study area	sparry arenaceous limestone	2.27	-10.71		Ji et al. (2020)
BP-4	this study area	Stratigulate dolostone	3.75	-9.07		Ji et al. (2020)
AD03-B	this study area	crystal powder dolomite	4.06	-8.51		Ji et al. (2020)
AD03-D	this study area	crystal powder dolomite	4.23	-7.90		Ji et al. (2020)
LP3-B1	this study area	fine-crystalline dolomite	3.21	-8.69		Ji et al. (2020)
LP5-B	this study area	fine-crystalline dolomite	3.02	-8.51		Ji et al. (2020)
LP8-B1	this study area	fine-crystalline dolomite	3.02	-8.94		Ji et al. (2020)
P13-B	this study area	fine-crystalline dolomite	3.46	-9.79		Ji et al. (2020)
GP18-Bb	this study area	fine-crystalline dolomite	4.26	-9.56		Ji et al. (2020)
BD16-B3	this study area	fine-crystalline dolomite	3.28	-9.13		Ji et al. (2020)
DT-257	this study area	fine-crystalline dolomite	2.30	-9.50		Ji et al. (2020)
DT-282	this study area	fine-crystalline dolomite	3.20	-8.90		Ji et al. (2020)
LE-2	this study area	meso-crystalline dolomite	2.40	-10.6		Ji et al. (2020)
AD03-B3	this study area	coarse-grained dolomite	3.30	-7.96		Ji et al. (2020)
BD30-1	this study area	coarse-grained dolomite	2.84	-10.12		Ji et al. (2020)
BD30-4	this study area	coarse-grained dolomite	3.38	-10.28		Ji et al. (2020)
BD30-5	this study area	coarse-grained dolomite	3.21	-9.80		Ji et al. (2020)
P11-B4	this study area	coarse-grained dolomite	3.86	-9.96		Ji et al. (2020)
GP20-B	this study area	coarse-grained dolomite	4.41	-8.84		Ji et al. (2020)
DT-224	this study area	coarse-grained dolomite	3.60	-7.90		Ji et al. (2020)
LE-1	this study area	coarse-grained dolomite	2.50	-8.7		Ji et al. (2020)
BG-10	this study area	coarse-grained dolomite	3.30	-8.10		Ji et al. (2020)
GL01-27	this study area	coarse-grained dolomite	3.10	-10.00		Ji et al. (2020)

(Continued on following page)



TABLE.3 (Continued) C- O and Sr isotope data for the different carbonate rocks in the Buqu Formation.

Sample ID	Sample position	Rock type	$\delta^{13}\text{C}\text{‰}_{\text{PDB}}$	$\delta^{18}\text{O}\text{‰}_{\text{PDB}}$	$^{87}\text{Sr}/^{86}\text{Sr}$	Remarks
GL01-33	this study area	coarse-grained dolomite	3.10	-10.40		Ji et al. (2020)
GL01-21	this study area	coarse-grained dolomite	3.10	-10.10		Ji et al. (2020)
Geluguanna	GLP section	saddle dolomite	4.29	-10.02		Ji et al. (2020)
Geluguanna	GLP section	saddle dolomite	3.36	-10.65		Ji et al. (2020)
Geluguanna	GLP section	saddle dolomite	3.49	-10.31		Ji et al. (2020)
Deruri	DRP section	saddle dolomite	3.22	-7.51		Ji et al. (2020)
	QZ12-232.16 m	sparry calcite veins	-1.15	-13.04		wan et al. (2020)
	QZ12-075.32 m	filled fractures	-1.18	-9.42		wan et al. (2020)
	QZ12-070.96 m		1.64	-10.75		wan et al. (2020)
16D-13	QZ12-075.22 m	micrite limestone	1.19	-8.25	0.707765	this study
16D-20	QZ12-130.83 m	micrite limestone	1.96	-8.62	0.707763	this study
16D-21	QZ12-131.46 m	sparry arenaceous limestone	2.57	-7.47	0.707850	this study
15S-2	SNP section	granular dolomite	3.75	-0.24		this study
15S-3	SNP section	granular dolomite	3.71	0.36		this study
15S-4	SNP section	granular dolomite	4.02	0.01		this study
15S-6	SNP section	granular dolomite	3.69	0.12		this study
15S-7	SNP section	granular dolomite	3.52	-0.47		this study
16D-14	QZ12-096.21 m	Rd1	3.42	-3.84	0.708176	this study
16D-07	QZ12-058.24 m	Rd1	3.74	-4.22	0.707747	this study
16D-25	QZ12-198.13 m	Rd1	4.23	-3.37	0.707654	this study
16D-06	QZ12-057.31 m	Rd2	4.11	-4.56	0.707525	this study
16D-15	QZ12-100.63 m	Rd2	3.64	-4.33	0.707667	this study
16D-17	QZ12-102.02 m	Rd2	3.18	-4.23	0.707572	this study
16D-22	QZ12-143.12 m	Rd2	3.33	-4.25	0.708037	this study
16D-23	QZ12-151.71 m	Rd2	3.83	-4.31	0.707686	this study
16D-02	QZ12-026.57 m	Rd3	4.42	-5.87	0.707432	this study
16D-03	QZ12-030.24 m	Rd3	4.18	-6.26	0.707609	this study
16D-05	QZ12-043.43 m	Rd3	3.95	-6.23	0.707990	this study
16D-16	QZ12-101.12 m	Rd3	3.28	-5.56	0.707780	this study
16D-24	QZ12-190.37 m	Rd3	2.72	-6.57	0.707593	this study
16D-01	QZ12-024.29 m	Rd4	3.24	-7.22	0.707303	this study
16D-04	QZ12-043.43 m	Rd4	4.05	-7.65	0.707884	this study
16D-10	QZ12-067.73 m	Rd4	3.92	-8.22	0.707752	this study
16D-12	QZ12-072.73 m	Rd4	3.85	-6.56	0.707234	this study
16D-18	QZ12-107.14 m	Rd4	4.14	-8.16	0.707593	this study
16D-27	QZ11-581.62 m	Rd4	3.68	-6.37	0.707865	this study
16D-19	QZ12-122.84 m	Cd1	3.02	-5.31	0.708147	this study
16D-08	QZ12-060.65 m	Cd2	-0.09	-10.41	0.708518	this study
16D-09	QZ12-060.64 m	Cd2	3.38	-9.58	0.708876	this study
16D-11	QZ12-069.33 m	Cd2	1.27	-9.25	0.708562	this study
16D-26	QZ11-580.95 m	Cd2	1.86	-8.56	0.708180	this study
QZ12-026	QZ12-105.02 m	Calcite cement filled dolomite intercrystalline pores	3.73	-5.38	0.707574	this study
QZ12-001-2	QZ12-232.16 m	Sparry calcite veins filled in fractures	-0.85	-11.97	0.708912	this study
QZ12-005	QZ12-219.76 m		-1.35	-11.33	0.709233	this study
QZ12-007	QZ12-219.81 m		0.57	-10.62	0.708128	this study
QZ12-013	QZ12-195.75 m		1.89	-10.45	0.708041	this study

## 5 Dolomite geochemistry

### 5.1 Fluid inclusion characteristics

Fluid inclusions are poorly developed in the dolomite of the Buqu Formation in the Qiangtang Basin (Table 2). Among the 33 thin sections of different dolomite samples, only 17 samples contain fluid inclusions. Fluid inclusions were identified in replaced dolomite and dolomite cement, including Rd2, Rd3, Rd4, Cd1, and Cd2, but not in Rd1. As described previously, misty centers and clear rims were observed in Rd2, Rd3, Rd4, and Cd2. The fluid inclusions in the healed trails in these dolomites were carefully avoided. The fluid inclusions that were isolated and in clusters in the misty center were interpreted to be of primary origin. In the clear rim, inclusions occurring along the boundary between the misty center and clear rim, as well as those in clusters, were interpreted to be of primary origin. These fluid inclusions in the misty center and clear rim were liquid-vapor inclusions with gas-liquid ratios of <10% and were chosen for further microthermometric analysis to reflect the diagenetic temperature and fluid salinity when they were captured (Liu, 1995; Braithwaite and Rizzi, 1997; Goldstein, 2001).

Among crystalline dolomites, the homogenization temperature of Rd2 types was low (lowest value 65.5°C), which is also the lowest homogenization temperature among the fluid inclusions observed in this study. Meanwhile, its ice-final melting temperature (−16.2°C) was also low. The highest homogenization temperature was 83°C, the average homogenization temperature was 73.24°C, and the lowest ice-final melting temperature was −20.1°C. The average corresponding salinity was 20.64%. The homogenization temperatures of the clear rim part of Rd2 dolomite ranged between 121.1 and 123.4°C (average 122.25°C). The ice-final melting temperatures were between −20.3°C and −20°C (average −20.15°C), with a corresponding salinity of 22.48%. While this study obtained only three fluid inclusion temperature measurements for the clear rim part of dolomite, which may not be statistically significant, these data indicated a higher formation temperature of the clear rim part of the dolomite compared to that of the misty center part.

The homogenization temperatures of fluid inclusions in Rd3 dolomite ranged from 82.9 to 98°C (average 90.18°C), slightly higher than those in Rd2 dolomite. Meanwhile, the ice-final melting temperatures, ranging from −19.7°C to −13°C (average −17.05°C), were also slightly higher than those in Rd2. The corresponding average salinity was 20.21%, slightly lower than that in Rd2. The homogenization temperatures of the clear rim part of Rd3 dolomite with “misty center and clear rim” were 102.8–157°C (average 126.75°C). The ice-final melting temperatures were between −21.1°C and −12.8°C (average of −17.8°C), with a corresponding salinity of 20.75%. These data indicated that the formation temperature of the clear rim part of Rd3 was higher than that of Rd3.

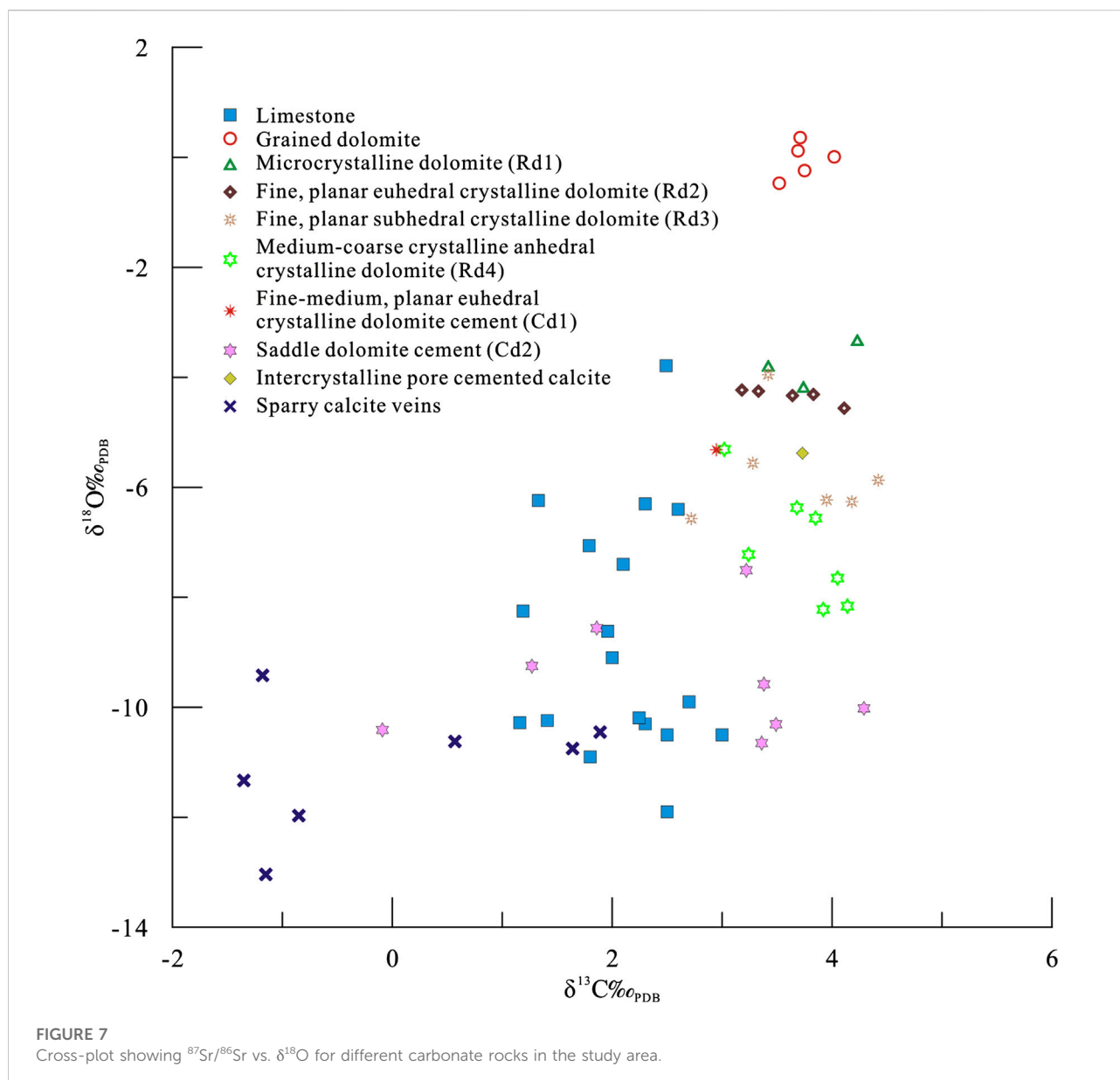
The homogenization temperatures of Rd4 dolomite inclusions were higher than those of Rd2 and Rd3, ranging from 84 to 117°C (average 102.67°C). The salinity ranged from −13.6 to −21.3°C (average −18.15°C), corresponding to an average salinity of 21.03%. The homogenization temperatures of the clear rim part of Rd4 dolomite with a “misty center and clear rim” were 118–145°C (average 130.15°C). The ice-final melting temperatures were between −21.5°C and −10°C (average −18.69°C), with a corresponding salinity of 21.37%. These indicated that the formation temperatures of the clear rim of Rd4 were higher than those of Rd4 and similar to those of Rd3 dolomite. The homogenization temperatures of the clear rim part of the Rd4 dolomite with a “misty center and clear rim” were generally higher than the maximum formation temperatures of granular dolomite, indicating that the formation environment of the clear rim might have been altered by a high-temperature environment during burial.

For dolomite fillings/cements, the homogenization temperatures of Cd1 partially coincided with those of Rd4, ranging from 110.2 to 116.7°C (average 113.5°C). The ice-final melting temperatures ranged from −20.1 to −19.9°C (average −20°C), corresponding to an average salinity of 22.38%. The homogenization temperatures of Cd2 differed significantly from those of crystalline dolomite and Cd1 filling, ranging from 121 to 165°C (average 140.43°C). Comparatively, the corresponding ice-final melting temperatures ranging from −20.9°C to −13.3°C did not differ significantly, indicating that the fluid properties of Cd2 were not significantly different from those of crystalline dolomite and Cd1. This may be related to the warming of tectonic thermal events under the background of tectonic compression. Under the microscope, part of Cd2 was broken into coarse near-regular rhomboid dolomite crystals with a “misty center and clear rim” structure. The homogenization temperatures of the fluid inclusions at the clear rim (between 89 and 119.4°C) were much lower than those of Cd2 but similar to those of Rd3. The ice-final melting temperature was similar to that of Cd2, with an average corresponding salinity of 21.06%. These also indicated that the genetic fluids in the clear rim of Cd2 did not involve meteoric water.

### 5.2 Isotope geochemical characteristics

#### 5.2.1 Oxygen and carbon isotope

Table 3 shows the carbon, oxygen, and strontium isotope data obtained in this study and the carbon and oxygen isotope data collected from published literature. The  $\delta^{13}\text{C}_{\text{‰PDB}}$  of micritic limestone in the Buqu Formation of Qiangtang Basin ranged from 1.16‰ to 3‰ (average 2.08‰) and the  $\delta^{18}\text{O}_{\text{‰PDB}}$  ranged from −11.9‰ to −3.79‰ (average −8.77‰). The carbon isotope  $\delta^{13}\text{C}_{\text{‰PDB}}$  of SNP grain dolomite (Figure 1A) was



3.52‰–4.02‰ (average 3.74‰). The oxygen isotope  $\delta^{18}\text{O}\text{‰PDB}$  was  $-0.47\text{‰}$ – $0.36\text{‰}$  (average  $-0.04\text{‰}$ ). The carbon isotope  $\delta^{13}\text{C}\text{‰PDB}$  of Rd1 ranged from 3.42 to 4.23‰ (average 3.8‰). The oxygen isotope  $\delta^{18}\text{O}\text{‰PDB}$  of Rd1 ranged from  $-4.22\text{‰}$  to  $-3.37\text{‰}$  (average  $-3.81\text{‰}$ ). The  $\delta^{13}\text{C}\text{‰PDB}$  ranged from 3.18 to 4.11‰ (average of 3.62‰) in Rd2 and varied from 2.72 to 4.42‰ (average 3.71‰). The oxygen isotope  $\delta^{18}\text{O}\text{‰PDB}$  of Rd3 ranged from  $-6.57\text{‰}$  to  $-5.56\text{‰}$  (average  $-6.10\text{‰}$ ). The  $\delta^{13}\text{C}\text{‰PDB}$  of medium-coarse anhedral dolomite (Rd4) ranged from 3.24 to 4.14‰ (average 3.81‰). The  $\delta^{18}\text{O}\text{‰PDB}$  ranged from  $-8.22\text{‰}$  to  $-6.37\text{‰}$  (average  $-7.36\text{‰}$ ).

The  $\delta^{13}\text{C}\text{‰PDB}$  and  $\delta^{18}\text{O}\text{‰PDB}$  of Cd1 were 3.02‰ and  $-5.13\text{‰}$ , respectively. The  $\delta^{13}\text{C}\text{‰PDB}$  of Cd2 ranged

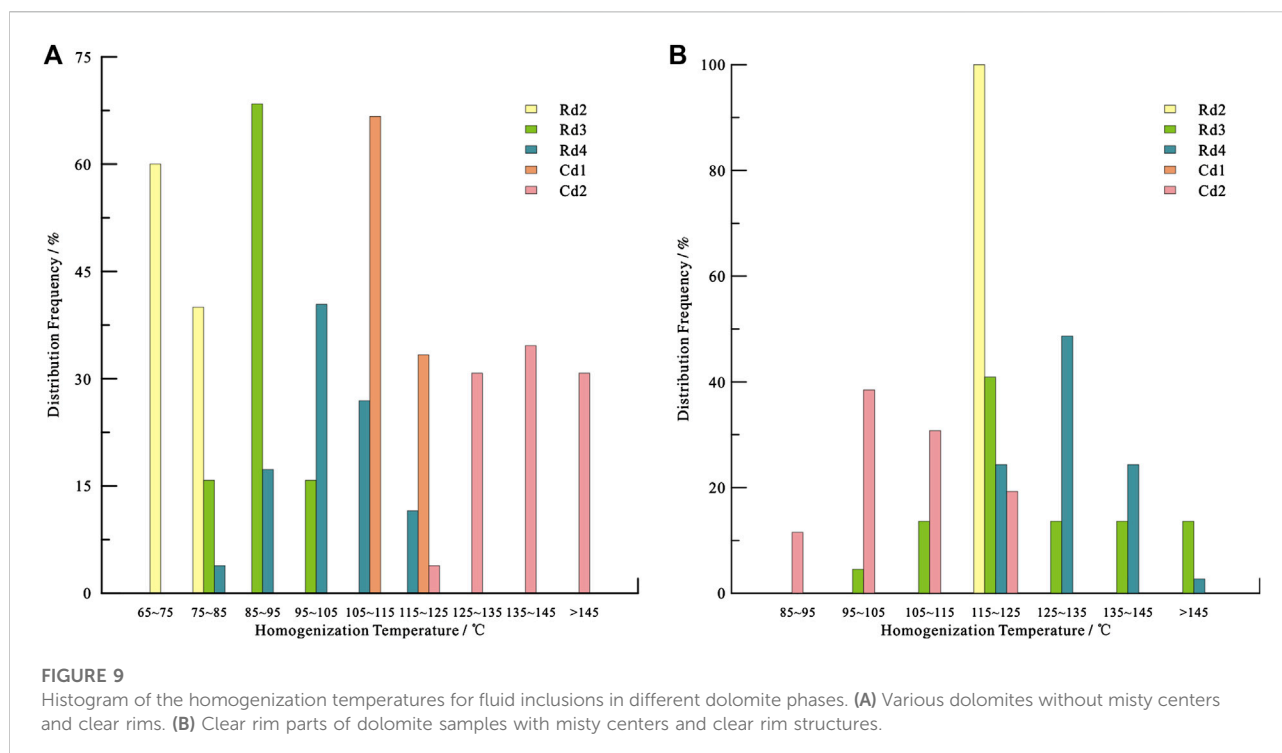
from  $-0.09$  to 3.38‰ (average 1.61‰), while the  $\delta^{18}\text{O}\text{‰PDB}$  ranged from  $-10.41\text{‰}$  to  $-8.56\text{‰}$  (average  $-9.45\text{‰}$ ). The calcite cement filling in the dolomite intercrystalline pores had a  $\delta^{13}\text{C}\text{‰PDB}$  of 3.73‰ and a  $\delta^{18}\text{O}\text{‰PDB}$  of  $-5.38\text{‰}$ . The sparry calcite veins filling the core fractures of well QZ12 had a  $\delta^{13}\text{C}\text{‰PDB}$  of between  $-1.35\text{‰}$  and  $-1.89\text{‰}$  (average  $-0.06\text{‰}$ ) and a  $\delta^{18}\text{O}\text{‰PDB}$  between  $-13.04\text{‰}$  and  $-9.42\text{‰}$  (average  $-11.08\text{‰}$ ).

### 5.2.2 Strontium isotope

Unlike C and O isotopes, Sr isotopes are not prone to fractionation or isotope exchange due to changes in biology, salinity, temperature, and pressure in geological history; thus, they are an effective tracer of carbonate diagenetic fluid (Huang







## 6 Discussion

### 6.1 Genesis of fabric well-preserved dolomite

Rd1 comprises fine dolomite that preserves the primary fabric of the precursor limestone. A fine dolomite grain can be interpreted as the result of dolomitization under near-surface, low temperature, and high salinity conditions (Gregg and Shelton, 1990). Moreover, fine-grained dolomite might be formed by consolidated or half-consolidated marls in metasomatism. Sibley et al. (1987) and Amthor and Friedman (1991) reported that the tiny grains had a larger surface area, which was favorable for rapid dolomite nucleation. Furthermore, a non-luminescence or uniform dark red ray under cathodoluminescence also reflected a marine diagenetic environment with very low manganese content (Huang et al., 2008), indicating the early formation of this type of dolomite. The well-preserved fabric of the precursor limestone might be related to mimetic metasomatism (Sibley, 1991) and lower diagenetic temperature (Machel, 2004). Metasomatism generally requires a high-density dolomite nucleus to ensure the preservation of the complex inner texture of calcium carbonate grains and cement (Sibley, 1991). The high-density nucleation was related to the highly soluble reactive and supersaturated dolomitization fluid. For instance, the bioclastic grain comprising high magnesium calcite was often first replaced by dolomite with a well-preserved primary fabric (Tucker and Wright, 1990).

Only a few fabric-well-preserved dolomites had developed and no associated evaporated salt was observed in the study area.

However, the granular dolomite was associated with evaporite in the Suonahu section. The freezing temperatures of fluid inclusions in the granular dolomites suggested a higher diagenetic fluid salinity, indicating high seawater salinity and large  $Mg^{2+}/Ca^{2+}$  ratios in the study area. These conditions are required for the formation of a highly saturated dolomitization fluid. The isotope geochemical data also supported this hypothesis. The  $^{87}Sr/^{86}Sr$  ratios of 0.707763–0.707850 were close to the contemporaneous seawater ratios (0.707–0.708) (Veizer et al., 1999) (Figure 7), whereas the C-O isotope values were significantly biased/shifted (Figure 8). The positive excursion of the C isotope values might be related to an evaporative environment as in such restricted and oxygen-deficient conditions, the degradation of isotopically light carbon from organic matter in the water would have been significantly inhibited (Mckenzie, 1981; Warren, 2000; Xiong et al., 2021, 2022). Rd1 is a mimetic replacement dolomite related to evaporated seawater in the contemporaneous or pencontemporaneous stage and resulted from high salinity seawater metasomatism formed by the strong evaporation of restricted water bodies in carbonate platforms under hot and arid-semiarid conditions (Pan et al., 2015).

### 6.2 Genesis of fabric poorly preserved or fabric-destructive dolomites

The straight crystal boundaries, loosely stacked saccharoidal crystals, uniform red-dark red cathodoluminescence, and deficient

stylolite of Rd2 indicated its formation before strong compaction and pressure solution. The homogenization temperatures of the fluid inclusions were low (65.5°C) and the freezing temperature indicated a salinity of 19.6% (Table 2; Figure 9A), suggesting that Rd2 was formed as a result of dolomitization at low temperature in the early diagenetic stage. The texture was similar to that of the typical dolomite formed by the backflow of high salinity evaporated seawater (Adams and Rhodes, 1960). Although associated evaporated salts did not develop in the dolostone of the Buqu Formation in the study area, the salinity of the fluid inclusions was 3–7 times higher than that of normal seawater (Table 2), indicating that seawater salinity might not reach the degree of large precipitation of evaporite when the dolomitization fluid was brackish water or mildly evaporated seawater. Therefore, it is difficult to explain the origin of such dolomite using the traditional hypersaline water backflow model. However, an increasing number of studies have shown the potential for dolomitization in medium salinity or mildly evaporated seawater (Whitaker and Smart, 1990; Qing et al., 2001). Similarly, in terms of isotopes, Rd2 showed slightly heavier oxygen isotope compositions than that of the contemporaneous marine calcite but similar strontium isotopes as that of contemporaneous seawater (Figure 7, Figure 8), indicating a correlation between its origin and slightly evaporated seawater. Medium salinity dolomitization fluid could also prevent excessive dolomitization favorable for the preservation of massive intercrystalline pores and the formation of loosely stacked saccharoidal crystals. Consequently, Rd2 was formed in a low-temperature environment in the early diagenetic stage. The backflow or infiltration diffusion of slightly evaporated seawater in the shallow burial stage might be the major mode of dolomitization, in which “appropriate” dolomitization was favorable for the development and preservation of the intercrystalline pores.

Rd3 has similar cathodoluminescence and O-Sr isotope compositions as those of Rd2, suggesting a similarity in their diagenetic environment and dolomitization fluid properties with predominant marine fluid in the shallow burial stage. Compared to Rd2, Rd3 had lighter O isotope compositions, related to the increased burial depth and temperature during its formation (Table 2; Figure 8, Figure 9A). With the increased burial depth, the continuous supply of dolomitization fluid and the increasing diagenetic temperature enabled dolomite to proceed to cementation accretion after it replaced calcite, resulting in excessive dolomitization. This excessive dolomitization led to the growth of new dolomite around the initially formed dolomite and the formation of enlarged rims or crustose zones, causing dolomite to transform from euhedral to subhedral crystal and intercrystalline pores to continuously decrease. However, Rd3 developed relatively straight crystal boundaries, indicating that the formation temperature did not reach the critical temperature for crystal curvature. Therefore, such dolomite was likely formed in the late shallow burial stage. The origins of Rd3 and Rd2 were similar and successive.

In the burial process, excessive dolomitization was the major reason for the less-euhedral crystals.

Rd4 mainly comprised nonplanar-curved anhedral dolomite, significantly different from the abovementioned dolomite in texture. Previous studies reported high formation temperature (Gregg and Sibley, 1984; Sibley and Gregg, 1987), highly saturated dolomitization fluid (Shukla, 1986), and competitive growth of crystals for growing space as factors leading to crystal curvature (Jones, 2005). The coarse grains, wavy extinction, and associated pressure solution stylolite indicated that Rd4 dolomite in the Buqu Formation in the Qiangtang Basin was formed with increasing temperature in the medium-deep burial stage (Fairchild, 1980; Qing and Mountjoy, 1989). The oxygen isotope of Rd4 was significantly negatively biased, and reduced by 2‰ compared to that of fine dolomite. The carbon isotope of Rd4 does not differ significantly compared to the abovementioned dolomite, which also indicated the correlation between its origin and high temperature (Figure 8, Figure 9). In particular, the  $^{87}\text{Sr}/^{86}\text{Sr}$  ratio was close to or slightly higher than that of contemporaneous seawater (Figure 7), indicating that no deep mantle source fluid or atmospheric freshwater participated in the formation of such dolomite. The slightly increasing Sr isotope ratios might be related to diagenetic alteration in the burial process (Qing et al., 1998) or the participation of a neutron-rich radioactive  $^{87}\text{Sr}$  fluid in the overlying or underlying clastic strata (Davies and Smith, 2006). Many high-temperature fluids participated in the formation of Rd4, as reflected by the homogenization temperatures of the fluid inclusions (average 102.67°C) and salinity of 21.03% (Table 2). In addition to the direct replacement of the precursor limestone, Rd4 might also be the result of recrystallization of the fine-grained dolomite formed at an early stage (Mazzullo, 1992; Hartig et al., 2011). Therefore, Rd4 was characterized by a bimodal granularity distribution. Moreover, the oxygen and strontium isotopes of some dolomite overlapped to different degrees, which might result from recrystallization due to the late dolomitization fluids alternating the early formed dolomite.

### 6.3 Genesis of dolomite filling

Cd1 often grew along the inwall of caverns and cracks as the first filling of caverns. Its crystal texture and cathodoluminescence were like those of fine-grained euhedral or subhedral dolomite. The freezing temperature and carbon and strontium isotopes of the fluid inclusions were also similar to those of thlarities, suggesting that Cd1 and fine-grained dolomite probably have a similar origin as that of fine-grained dolomite. These were similar to those of dolomitization fluid. However, the homogenization temperature of Cd1 was higher than that of fine-grained euhedral or subhedral dolomites and the oxygen isotope was negatively skewed compared to that of fine-grained or medium- to coarse-grained dolomites (Table 2; Figure 8,

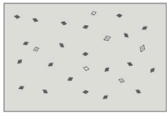
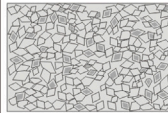
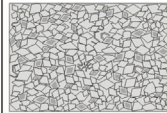
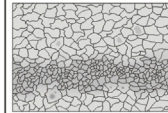

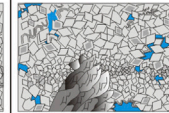
Dolomite type	Matrix dolomite				Void-filling Dolomite/Dolomite Cement	
	Rd1	Rd2	Rd3	Rd4	Cd1	Cd2
Crystal size	micrite/ microcrystal	fine grain/ fine crystalline	fine grain/ fine crystalline	medium to coarse grained	fine grain/ fine crystalline	medium to coarse grained
Crystal type		euhedral	subhedral	anhedral	euhedral	anhedral saddle
Crystal surface morphology	planar	planar	planar	planar-curved	planar	curved
Contact relationship between crystals		point	point-line	concavo-convex	point-line	concavo-convex
Pore abundance	very poor	well	well to medium	medium to poor	poor	poor
Genetic mechanism	metasomatic genesis	metasomatic genesis	metasomatic genesis	metasomatic genesis / recrystallization	recrystallization	hydrothermal origin
Developmental stage	penecontemporaneous	shallow buried	late shallow burial	middle to deep burial	late shallow burial	tectonic thermal event (79.03Ma B. P.)
Schematic diagram of crystal texture						

FIGURE 10

Model showing the evolution of diagenetic fabrics among representative dolomites from the study area.

Figure 9), indicating that Cd1 experienced diagenetic transformations such as recrystallization in the deep burial stage, where the higher formation temperature resulted in the fractionation of heavy oxygen isotopes.

The unique crystal texture of Cd2 indicated a unique growing environment. The crystallographic and geochemical features illustrated that such a crystal was rapidly formed in a highly supersaturated solution (Searl, 1989), but a small quantity of Cd2 might be related to the self-regulation effect of the host dolomite (Qing and Chen, 2010) and thermochemical sulfate reduction in the burial and compaction process (Machel, 1987; Machel and Lonnee, 2002). The dolomite in the Qiangtang Basin has higher homogenization temperatures compared to the saddle-shaped dolomite with limestone as the host mineral in North America and salinity of nearly 7 times higher than the contemporaneous seawater, indicating the formation was related to thermal fluids (Wang et al., 2010). However, dolomite in the Qiangtang basin, in general, might be formed by the recrystallization of previous matrix dolomite or directly in a thermal fluid rather than by replacing limestone. The Cd2 in the Tarim Basin formed during the Cambrian–Ordovician periods has similar oxygen and strontium isotopes as Rd4, and the saddle-shaped dolomite of the Buqu Formation in the Qiangtang Basin has similar carbon isotopes as grained dolomite. However, Cd2 has higher strontium isotopes but significantly lower (2‰) oxygen isotope than that of medium-coarse-grained dolomite (Figures 7, 8). These results further indicate that the saddle-shaped dolomite fillings (Cd2) in the

Buqu Formation dolomite in the Qiangtang Basin were formed with the participation of external thermal fluids.

If the foreign fluid was from the deep mantle-derived fluids, the saddle-shaped dolomite formed should be characterized by a low  $^{87}\text{Sr}/^{86}\text{Sr}$  ratio. If the saddle dolomite flowed through the  $^{87}\text{Sr}$ -rich clastic rocks of the Lower Fuqu and Sewa formations, it would have absorbed a large amount of  $^{87}\text{Sr}$  and showed an increased  $^{87}\text{Sr}/^{86}\text{Sr}$  ratio in the foreign fluid. However, this is inconsistent with our findings of lower  $^{87}\text{Sr}/^{86}\text{Sr}$  ratios but a wider range in the saddle dolomite compared to those of the matrix dolomite (Table 3; Figure 7). In addition, the distribution range and average ice-final melting temperature of saddle-shaped dolomite were similar to those of Rd3 and Rd4, indicating the saddle-shaped dolomite fluid was a contemporaneous marine fluid trapped in the Buqu Formation without the involvement of atmospheric water. The Yanshan and Himalayan tectonic movements occurred after the Jurassic deposition in the Qiangtang Basin. The Yanshan Movement formed the intrusive rocks (Andesite?-porphyrite) in the Buqu Formation of the SBJP section, which may have provided a heat source for saddle dolomite genetic fluid. The tectonic compression then drove the movement of marine fluid trapped in the Buqu Formation. During this migration, the marine fluid passed through the  $^{87}\text{Sr}$ -enriched clastic strata of the overlying Xiali Formation, the underlying the Quse Formation, and the Sewa Formation. A schematic diagram of the evolution of dolomite texture in the study area of the Qiangtang basin is shown in Figure 10.

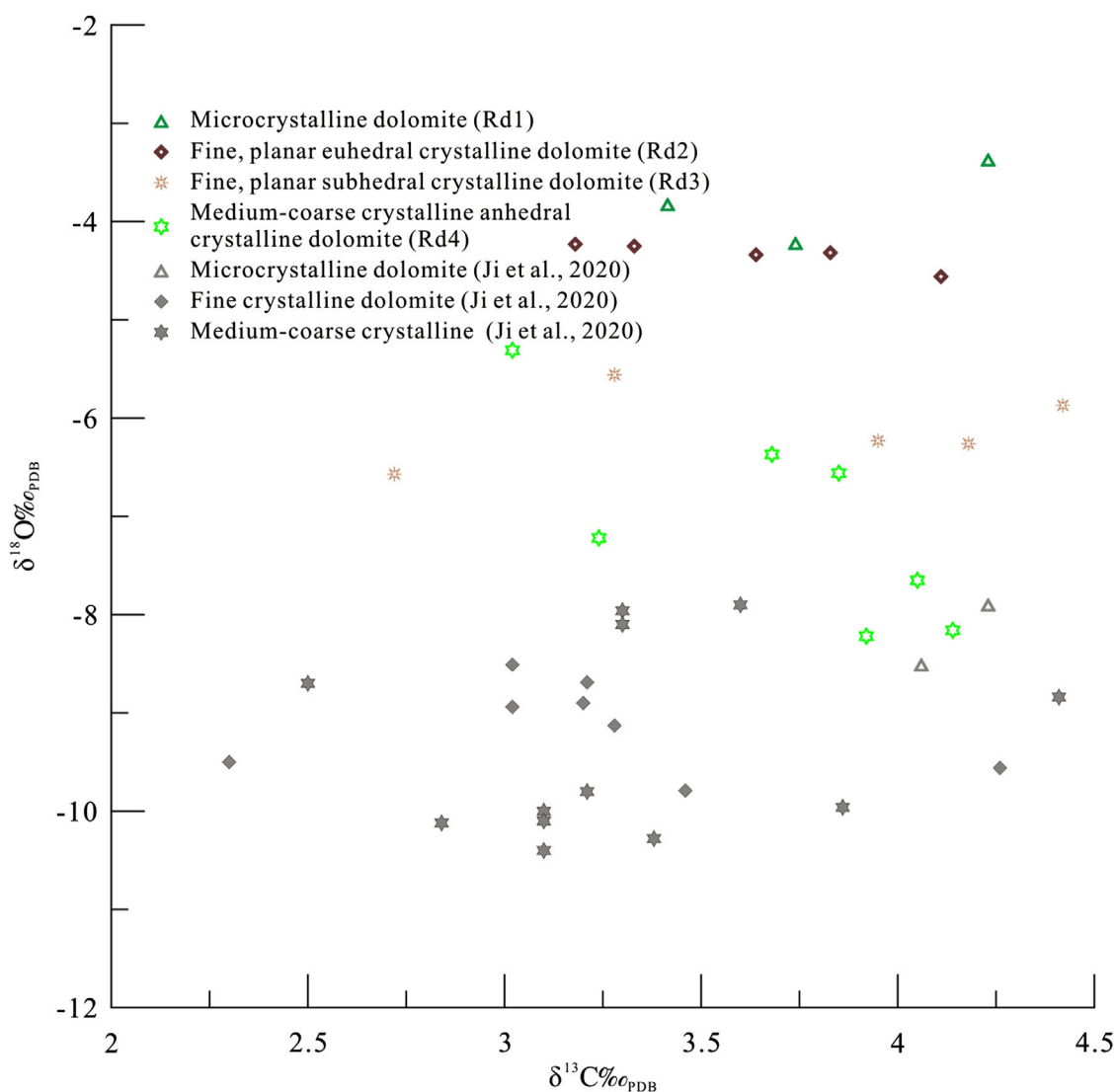


FIGURE 11

Comparisons of cross-plots showing  $\delta^{18}\text{O}$  vs.  $\delta^{13}\text{C}$  for different types of dolomite without misty centers and clear rims with previous research results.

## 6.4 Revelation of the misty center and clear rim

The granular dolomite and broken saddle dolomite in the study area in the Buqu Formation area tended to show a misty center and clear rim structure (Figure 2A). Dolomite crystals with clear rims have higher fluid formation temperatures compared to dolomite without the misty center and clear rim structure (Table 2; Figure 9B), or even higher than Rd4 and Cd2. Thus, the clear rim formation of the granular dolomite of the Buqu Formation was related to tectonic thermal events. The ice-final melting temperatures and corresponding salinity of the fluids forming the clear rim of the grain dolomite barely varied, indicating that these fluids were

tectonic thermal fluids. The formation time was consistent with that of Cd2, indicating that tectonothermal events related to Cd2 significantly impacted the early dolomites, especially oxygen isotopic composition (Figure 11). The tectonothermal events may have caused high-temperature heat transfer fluid in the early dolomite oxygen isotope fractionation. The clear rim of dolomite formed in the high-temperature thermal fluid flow showed lower oxygen isotopic values, resulting in the lower oxygen isotope values of the dolomite with clear rim structures compared to those of the dolomite without misty center clear rim structures.

Two tectonic activities in the Yanshan and Himalayan periods occurred after the deposition of Jurassic strata in the Qiangtang Basin (Fang et al., 2002), especially the late Cretaceous Yanshan



Movement (Act II) that produced many thrust nappe structures (Wu et al., 2014, 2016; Ji et al., 2019; Zhao Z. et al., 2020; Wan et al., 2021). Broken after a nearly perfect diamond saddle dolomite, the clear rim portion of the fluid inclusions has a homogenization temperature far below the formation temperature of the saddle dolomite (Table 2; Figure 9). The clear rim of the saddle dolomite formed later than the saddle dolomite, and the corresponding freezing temperature and salinity suggest that the saddle dolomite was broken. During this period, the fault lines that connect atmospheric water were not formed and atmospheric freshwater did not infiltrate the Buqu Formation, suggesting that the ancient oil reservoir was not destroyed at this time. Zircon U-Pb dating of andesitic porphyrite in the SBJP section of the Buqu Formation in the northern part of the study area (Figure 1B) determined the ages for the first time at 78–64 Ma B. P. (Wan et al., 2018a; Wan et al., 2020; Wan et al., 2021). Our latest research determined the intrusive age of andesitic porphyrites in this section of 79.03 Ma (this will be described separately in other articles), indicating that the saddle-shaped dolomite was formed at about 79.03 Ma and was possibly related to the intraplate-collision orogeny between the Lhasa and Qiangtang terranes. Moreover, U-Pb isotope (LA-ICP-MS) dating of saddle-shaped dolomite showed (Qiao et al., 2020; Qiao et al., 2021a) that the saddle-shaped dolomite was formed at about 80 Ma B. P. (This will be described separately in other articles), further confirming that the saddle-shaped dolomite was formed during the late stage of early the Cretaceous. All these data support that the formation of the paleo-reservoirs of oil in the southern Qiangtang Depression was related to the collision between the Indian subcontinent and the Eurasian plate and the uplift of the Qinghai-Tibet Plateau in the Cenozoic.

## 7 Conclusion

- 1) According to the primary fabric of the precursor limestone, the dolostone of the Buqu Formation in the Qiangtang Basin is divided into fabric-well-preserved (residual) and fabric-poorly preserved or fabric-destructive dolomite. The fabric-well-preserved dolomite is mainly residual dolomite (Rd1) consisting of muddy-silty crystals. The other dolomites include fine-grained euhedral dolomite (Rd2), fine-grained subhedral dolomite (Rd3), and medium-to coarse-grained anhedral dolomite (Rd4). In addition, two types of dolomite fillings developed in the study area: fine-grained euhedral-subhedral dolomite filling (Cd1) and medium-to coarse-grained saddle-shaped dolomite filling (Cd2).
- 2) Rd1 was formed in the penecontemporaneous stage as a result of mimetic metasomatism related to seawater evaporation. The flow of massive highly saturated dolomitization fluids was favorable for the preservation of the primary fabric. Among the fabric-poorly preserved or fabric-destructive dolomite, Rd2 and Rd3 were formed in a low-temperature environment at the shallow burial stage. The backflow or

infiltration diffusion might be the major driving mechanism of dolomitization fluids. Moderate dolomitization was favorable for the formation and preservation of holes, whereas excessive dolomitization resulted in the transformation from euhedral to subhedral crystals and gradually blocked holes. Medium-coarse-grained anhedral dolomite was mostly related to high temperature and recrystallization in the medium-deep burial stage and the higher formation temperature of curved crystals.

- 3) Cd1 was formed in the shallow burial stage. Cd2 was related to the collisional orogeny between the Lhasa and Qiangtang terranes in the late Early Cretaceous (79.03 Ma). The thermal fluid was the marine fluid trapped in the overlying and underlying clastic rocks driven by the tectonothermal event during this period. Cd2 was mainly formed by recrystallization or direct precipitation from thermal fluids.
- 4) The tectonothermal events of the late Early Cretaceous greatly influenced the dolomites formed in the early stage, leading to the development of the clear rim with a misty center. The geochemical characteristics of the clear rim structure that formed after the fracture of saddle-shaped dolomites indicate that the formation of the southern Qiangtang oil paleo-reservoir belt was related to the Himalayan movement.

## Data availability statement

The raw data supporting the conclusions of this article will be made available by the authors, without undue reservation.

## Author contributions

All authors listed have made a substantial, direct, and intellectual contribution to the work and approved it for publication.

## Funding

This article was funded by the National Natural Science Foundation of China (“The mechanism of pores formation and preservation during dolomitization: a case study from Buqu formation dolomite reservoirs, Southern Qiangtang depression”, No. 41902138).

## Conflict of interest

The authors declare that the research was conducted in the absence of any commercial or financial relationships that could be construed as a potential conflict of interest.

Reviewer XT declared a shared affiliation with author JW to the handling editor at the time of review

## Publisher's note

All claims expressed in this article are solely those of the authors and do not necessarily represent those of their affiliated

## References

- Adams, J. E., and Rhodes, M. L. (1960). Dolomitization by seepage refluxion. *AAPG Bull.* 44 (12), 1912–1920. doi:10.1306/0bda6263-16bd-11d7-8645000102c1865d
- Amthor, J. E., and Friedman, G. M. (1991). Dolomite-rock textures and secondary porosity development in Ellenburger Group carbonates (Lower Ordovician), west Texas and southeastern New Mexico. *Sedimentology* 38 (2), 343–362. doi:10.1111/j.1365-3091.1991.tb01264.x
- Badiozamani, K. (1973). The dorag dolomitization model, application to the middle Ordovician of Wisconsin. *J. Sediment. Res.* 43 (4), 965–984. doi:10.1306/74d728c9-2b21-11d7-8648000102c1865d
- Bi, Y. Q., Tian, H. Q., Zhao, Y. S., Ma, Y. X., Yu, W. Q., and Hu, S. Y. (2001). On the micrite envelope to restoration of primary texture character of secondary dolomites and its significance. *Acta Petrol. Sin.* 17 (3), 491–496.
- Braithwaite, C. J. R., and Rizzi, G. (1997). The geometry and petrogenesis of hydrothermal dolomites at Navan, Ireland. *Sedimentology* 44 (3), 421–440. doi:10.1046/j.1365-3091.1997.d01-30.x
- Chen, H., Chen, M., Sun, W., and Wang, Y. K. (2018). Sedimentary facies and palaeogeography of the middle jurassic Buqu formation in the longeni - esima ancient oil reservoirs zone, Qiangtang basin, northern xizang. *Geol. Tethyan Geol.* 38 (2), 74–81. (in Chinese with English abstract).
- Chen, M., Sun, W., Chen, H., and Song, C. Y. (2020). Sedimentary characteristics and oil-gas geological significance of the middle jurassic Buqu formation in the ersma area, southern Qiangtang basin, tibet. *Geol. Tethyan Geol.* 40 (3), 96–101. (in Chinese with English abstract).
- Chen, W. B., Yang, P., Zhang, Y. J., and Peng, Z. M. (2006). Dolostone reservoirs and their Genesis in the Zaring oil pool in southern Qiangtang Basin. *Sediment. Geol. Tethyan Geol.* 26 (2), 43–46. (in Chinese with English abstract).
- Choquette, P. W., and Steinen, R. P. (1980). Mississippian non-supratidal dolomite, ste. Genevieve limestone, Illinois basin: Evidence for mixed-water dolomitization. doi:10.21110/pec.80.28.0163
- Dai, J. X., Ni, Y. Y., Dong, D. Z., Qin, S. F., Zhu, G. Y., Huang, S. P., et al. (2021). 2021-2025 is a period of great development of China's natural gas industry: Suggestions on the exploration and development of natural gas during the 14th five-year plan in China. *J. Nat. Gas Geoscience* 6 (4), 183–197. doi:10.1016/j.jnggs.2021.08.001
- Dai, X. F., Du, B. Q., Zhang, M., Li, J., Tang, T. K., Xu, Y. P., et al. (2020). Reunderstanding and significance of high-quality reservoirs of the inner dengying Formation in the anyue gas field. *Nat. Gas. Ind. B* 7 (2), 109–119. doi:10.1016/j.ngib.2020.03.001
- Davies, G. R., and Smith, L. B., Jr (2006). Structurally controlled hydrothermal dolomite reservoir facies: An overview. *Am. Assoc. Pet. Geol. Bull.* 90 (11), 1641–1690. doi:10.1306/05220605164
- Dolomieu, D. D. (1981). Sur un genre de Pierres calcaires tres-peu effervescentes avec les Acides, & phosphorescentes par la collision. *J. Phys.* 29 (1), 4–10. 3–10. Translation of Dolomieu's paper with notes reporting his discovery of dolomite by Carozzi, A. V. & Zenger, D.H. 1981. Journal of Geological Education. 29. doi:10.5408/0022-1368-29.1.4
- Fairchild, I. J. (1980). Stages in a precambrian dolomitization, scotland: Cementing versus replacement textures. *Sedimentology* 27 (6), 631–650. doi:10.1111/j.1365-3091.1980.tb01652.x
- Fang, X. M., Lu, B., Liu, C. Y., and Liu, Z. (2002). Evolution of the central dome in the Qiangtang basin and its importance in oil-gas exploration. *Geol. Rev.* 48 (3), 279–283. (in Chinese with English abstract). doi:10.16509/j.georeview.2002.03.010
- Friedman, G. M. (1965). Terminology of crystallization textures and fabrics in sedimentary rocks. *J. Sediment. Res.* 35 (3), 643–655. doi:10.1306/74d7131b-2b21-11d7-8648000102c1865d
- Fu, L., Li, J. Z., Xu, W. L., Guo, W., Li, N. X., Zhang, Y. Q., et al. (2021). Characteristics and main controlling factors of Ordovician deep subsalt reservoir in central and eastern Ordos Basin, China. *J. Nat. Gas Geoscience* 6 (1), 13–25. doi:10.1016/j.jnggs.2021.03.001
- Goldstein, R. H. (2001). Fluid inclusions in sedimentary and diagenetic systems. *Lithos* 55 (1-4), 159–193. doi:10.1016/s0024-4937(00)00044-x
- Gregg, J. M., and Shelton, K. L. (1990). Dolomitization and dolomite neomorphism in the back reef facies of the Bonnetterre and Davis formations (Cambrian), southeastern Missouri. *J. Sediment. Res.* 60 (4), 549–562. doi:10.1306/212f91e2-2b24-11d7-8648000102c1865d
- Gregg, J. M., Shelton, K. L., Johnson, A. W., Somerville, I. D., and Wright, W. R. (2001). Dolomitization of the waulsortian limestone (lower carboniferous) in the Irish midlands. *Sedimentology* 48 (4), 745–766. doi:10.1046/j.1365-3091.2001.00397.x
- Gregg, J. M., and Sibley, D. F. (1984). Epigenetic dolomitization and the origin of xenotopic dolomite texture. *J. Sediment. Res.* 54 (3), 908–931. doi:10.1306/212f8535-2b24-11d7-8648000102c1865d
- Guo, X. S., Hu, D. F., Huang, R. C., Wei, Z. L., Duan, J. H., Wei, X. F., et al. (2020). Deep and ultra-deep natural gas exploration in the Sichuan Basin: Progress and prospect. *Nat. Gas. Ind. B* 7 (2), 419–432. doi:10.1016/j.ngib.2020.05.001
- Hanshaw, B. B., Back, W., and Deike, R. G. (1971). A geochemical hypothesis for dolomitization by ground water. *Econ. Geol.* 66 (5), 710–724. doi:10.2113/gsecongeo.66.5.710
- Hartig, K. A., Soreghan, G. S., Goldstein, R. H., and Engel, M. H. (2011). Dolomite in Permian paleosols of the Bravo Dome CO2 Field, USA: Permian reflux followed by late recrystallization at elevated temperature. *J. Sediment. Res.* 81 (4), 248–265. doi:10.21110/jsr.2011.24
- Huang, B., Zhang, S., Lu, Z., Ye, N., Zhu, B., Ding, X., et al. (2021). Origin of dolomites in lower-middle ordovician carbonate rocks in the yingshan formation, gucheng area, Tarim Basin: Evidence from petrography and geochemical data. *Mar. Petroleum Geol.* 134, 105322. doi:10.1016/j.marpetgeo.2021.105322
- Huang Q Y.Zhang, S. N., Zhang, S. Y., Liu, D., and Ye, N. (2014). Textural control on the development of dolomite reservoir: A study from the cambrian-ordovician dolomite, central Tarim Basin, NW China. *Nat. Gas. Geosci.* 25 (3), 341–350. (in Chinese with English abstract).
- Huang, S. J., Lü, J., and Lan, Y. F. (2011). The main texture of dolomite of middle permian, Western Sichuan Basin: Concurrently on the differences with upper permian-triassic, northeast Sichuan Basin. *Acta Petrol. Sin.* 27 (8), 2253–2262.
- Huang, S., Huang, K., Lü, J., and Lan, Y. (2014). The relationship between dolomite textures and their formation temperature: A case study from the permian-triassic of the Sichuan Basin and the lower paleozoic of the Tarim Basin. *Pet. Sci.* 11 (1), 39–51. doi:10.1007/s12182-014-0316-7
- Huang, S. J., Qing, H. R., Hu, Z. W., Pei, C. R., Wang, Q. D., Wang, C. M., et al. (2008). Cathodoluminescence and diagenesis of the carbonate rocks in feixianguan formation of triassic, eastern Sichuan Basin of China. *Earth Science—Journal China Univ. Geosciences* 33 (1), 26–34.
- Ji, C. J., Chen, C., Wu, Z. H., Yi, H. S., Xia, G. Q., and Zhao, Z. (2020). Carbon and oxygen isotopes analysis of the fluid inclusions in Middle Jurassic saccharoidal dolostone of Qiangtang Basin and discussion on the Genesis of dolostone. *Geol. Rev.* 66 (5), 1186–1198. (in Chinese with English abstract).
- Ji, C. J., Wu, Z. H., Liu, Z. W., and Zhao, Z. (2019). Structural features of thrust nappes in the Qiangtang basin and hydrocarbon resources effect. *J. Geomechanics* 25 (S1), 66–71. (in Chinese with English abstract).
- Jones, B. (2005). Dolomite crystal architecture: Genetic implications for the origin of the tertiary dolostones of the Cayman Islands. *J. Sediment. Res.* 75 (2), 177–189. doi:10.21110/jsr.2005.014
- Jones, G. D., Smart, P. L., Whitaker, F. F., Rostron, B. J., and Machel, H. G. (2003). Numerical modeling of reflux dolomitization in the Grosmont platform complex (Upper Devonian), Western Canada sedimentary basin. *Am. Assoc. Pet. Geol. Bull.* 87 (8), 1273–1298. doi:10.1306/03260302007
- Kaldi, J., and Gidman, J. (1982). Early diagenetic dolomite cements; examples from the permian lower magnesian limestone of england and the pleistocene carbonates of the Bahamas. *J. Sediment. Res.* 52 (4), 1073–1085. doi:10.1306/212f80da-2b24-11d7-8648000102c1865d

- Land, L. S. (1985). The origin of massive dolomite. *J. Geol. Educ.* 33 (2), 112–125. doi:10.5408/0022-1368-33.2.112
- Li, X., Yi, H. S., Jin, F., Ji, C. J., and Li, K. Y. (2018). Diagenetic characteristics of dolomite in the Long'en-Angdar Co ancient reservoir, Qiangtang Basin, China. *J. Chengdu Univ. Technol. Sci. Technol. Ed.* 45 (2), 142–153. (in Chinese with English abstract).
- Liu, D. H. (1995). Fluid inclusion studies: An effective means for basin fluid investigation. *Earth Sci. Front.* 2 (4), 149–154. (in Chinese with English abstract).
- Liu, J. Q., Chen, W. B., Yang, P., Chen, W. X., and Fu, X. G. (2008a). The dolomite fabric characteristics and lead isotope significance of the ancient oil accumulation in Long'en-angdar lake Qiangtang basin. *Acta Geosci. Sin.* 29 (1), 72–80. (in Chinese with English abstract).
- Liu, J. Q., Chen, W. B., Yang, P., Chen, W. X., and Fu, X. G. (2008b). The Longeni-Aangdaerco paleo-oil dolomite geochemical characteristics in southern part of the center uplift zone of Qiangtang basin and its significance. *Acta Petrol. Sin.* 24 (06), 1379–1389. (in Chinese with English abstract).
- Liu, J. Q., Jia, B. J., Yang, P., Chen, W. B., Chen, W. X., and Fu, X. G. (2008c). Characteristics of the paleo-oil dolomite REE geochemistry of Buqu formation in southern part of the central uplift zone of Qiangtang basin and its significance. *Acta Sedimentol. Sin.* 26 (1), 28–38. (in Chinese with English abstract).
- Liu, J. Q., Yang, P., Chen, W. B., Chen, W. X., and Fu, X. G. (2010). The characteristics of Longen-i Angdaerco paleo-oil dolomite in southern part of the central uplift zone of Qiangtang Basin and its forming mechanism, China University of Geosciences (Beijing):Peking University. *Earth Sci. Front.* 17 (1), 311–321. (in Chinese with English abstract).
- Liu, X. Y., Wei, L. B., Liu, B. X., Zhang, L., Guo, W., Zhang, J. W., et al. (2021). Characteristics of natural gas accumulation in the Cambrian weathered crust in southwestern Ordos Basin. *Nat. Gas. Ind. B* 8 (5), 421–430. doi:10.1016/j.ngib.2021.08.001
- Long, S. X., Cheng, Z., Xu, H. M., and Chen, Q. (2020). Exploration domains and technological breakthrough directions of natural gas in SINOPEC exploratory areas, Sichuan Basin, China. *J. Nat. Gas Geoscience* 5 (6), 307–316. doi:10.1016/j.jnggs.2020.10.002
- Lonnee, J., and Machel, H. G., 2004. Dolomitization by halite-saturated brine and subsequent hydrothermal alteration in the devonian slave point formation, clark lake gas field, British columbia. In CSPG-CHOA-CWLS Joint Conference Abstracts (Vol. 13).
- Lu, F. F., Tan, X. C., Zhong, Y., Luo, B., Zhang, B. J., Zhang, Y., et al. (2020). Origin of the penecontemporaneous sucrosic dolomite in the Permian Qixia formation, northwestern Sichuan Basin, SW China. *Petroleum Explor. Dev.* 47 (6), 1218–1234. doi:10.1016/s1876-3804(20)60131-3
- L'opez-Horgue, M. A., Iriarte, E., Schröder, S., Fernández-Mendiola, P. A., Caline, B., Corneylie, H., et al. (2010). Structurally controlled hydrothermal dolomites in Albian carbonates of the Asón valley, Basque Cantabrian Basin, Northern Spain. *Mar. Petroleum Geol.* 27 (5), 1069–1092. doi:10.1016/j.marpetgeo.2009.10.015
- Machel, H. G. (2004). Concepts and models of dolomitization: A critical reappraisal. *Geol. Soc. Lond. Spec. Publ.* 235 (1), 7–63. doi:10.1144/gsl.sp.2004.235.01.02
- Machel, H. G., and Lonnee, J. (2002). Hydrothermal dolomite a product of poor definition and imagination. *Sediment. Geol.* 152 (3–4), 163–171. doi:10.1016/s0037-0738(02)00259-2
- Machel, H. G. (1987). Saddle dolomite as a by-product of chemical compaction and thermochemical sulfate reduction. *Geol.* 15 (10), 936. doi:10.1130/0091-7613(1987)15<936:sdaabo>2.0.co;2
- Mazzullo, S. J. (1992). Geochemical and neomorphic alteration of dolomite: A review. *Carbonates Evaporites* 7 (1), 21–37. doi:10.1007/bf03175390
- Mckenzie, J. A. (1981). Holocene dolomitization of calcium carbonate sediments from the coastal sabkhas of abu dhabi, UAE: A stable isotope study. *J. Geol.* 89, 185–198. doi:10.1086/628579
- McKenzie, J. A., Hsu, K. J., and Schneider, J. F. (1980). Movement of subsurface waters under the sabkha Abu Dhabi, UAE, and its relation to evaporative dolomite Genesis. *Concepts Models Dolomitization*, 11–30. doi:10.2110/pec.80.28.0011
- Morrow, D. (1998). Regional subsurface dolomitization: Models and constraints. *Geosci. Can.*
- Mountjoy, E. W., Machel, H. G., Green, D., Duggan, J., and Williams-Jones, A. E. (1999). Devonian matrix dolomites and deep burial carbonate cements: A comparison between the rimbey-meadowbrook reef trend and the deep basin of west-central alberta. *Bull. Can. Petroleum Geol.* 47 (4), 487–509.
- Mutti, M., and Simo, J. A. (1994). Distribution, petrography and geochemistry of early dolomite in cyclic shelf facies, Yates Formation (Guadalupian), Capitan Reef Complex, USA. Dolomites. *A Volume Honour Dolomieu*, 91–107. doi:10.1002/9781444304077.ch7
- Pan, J. Q., Song, C. H., Bao, J., Ma, L. F., Yan, M. D., Fang, X. M., et al. (2015). Geochemical characteristics and salt-forming analysis of jurassic strata in Qiangtang basin. *Acta Geol. Sin.* 89 (11), 2152–2160. (in Chinese with English abstract).
- Patterson, R. J., and Kinsman, D. J. J. (1982). Formation of diagenetic dolomite in coastal sabkha along Arabian (Persian) Gulf. *AAPG Bull.* 66 (1), 28–43.
- Peng, Z. M., Liao, Z. L., Chen, M., Liu, J. Q., Zhang, Y. J., Chen, W. B., et al. (2008). Origin of the jurassic dolostone reservoirs in the Qiangtang basin on the qinghai-xizang plateau. *Geol. Tethyan Geol.* 28 (4), 1–6. (in Chinese with English abstract).
- Purser, B., Tucker, M., and Zenger, D. (1994). Dolomites. International association of sedimentologists. Oxford: Blackwell Scientific Publications, 451.
- Qiao, Z. F., Shao, G. M., Luo, X. Y., Cao, P., Sun, X. W., and Shen, A. J. (2021a). Genetic classification and large-scale reservoir development law of burial dolomite: Cognition based on LA-ICP-MS trace elemental mapping and U-Pb dating. *Nat. Gas. Ind.* 41 (9), 46–56. (in Chinese with English abstract).
- Qiao, Z. F., Zhang, S. N., Shen, A. J., Hu, A. P., Liang, F., Luo, X. Y., et al. (2020). Laser ablate U-Pb dating-based determination of burial dolomitization process: A case study of lower ordovician penglaiba formation of yonganba outcrop in Tarim Basin. *Acta petrol. Sinia* 36 (11), 3493–3509. (in Chinese with English abstract).
- Qiao, Z. F., Zhang, S. N., Shen, A. J., Shao, G. M., She, M., Cao, P., et al. (2021b). Features and origins of massive dolomite of lower ordovician penglaiba Formation in the northwest Tarim Basin: Evidence from petrography and geochemistry. *Petroleum Sci.* 18, 1323–1341. doi:10.1016/j.petsci.2021.03.001
- Qing, H. R., and Chen, D. Z. (2010). Non-hydrothermal saddle dolomite: Petrological and geochemical evidence from the ordovician yeoman formation, southeastern saskatchewan, canada. *Acta Sedimentol. Sin.* 28 (5), 980–986.
- Qing, H. R., Barnes, C. R., Buhl, D., and Veizer, J. (1998). The strontium isotopic composition of ordovician and silurian brachiopods and conodonts: Relationships to geological events and implications for coeval seawater. *Geochimica cosmochimica acta* 62 (10), 1721–1733. doi:10.1016/s0016-7037(98)00104-5
- Qing, H. R., Bosence, D. W. J., and Rose, E. P. F. (2001). Dolomitization by penesaline sea water in Early Jurassic peritidal platform carbonates, Gibraltar, Western Mediterranean. *Sedimentology* 48 (1), 153–163. doi:10.1046/j.1365-3091.2001.00361.x
- Qing, H. R., and Mountjoy, E. W. (1989). Multistage dolomitization in rainbow buildups, middle devonian keg river formation, alberta, Canada. *J. Sediment. Res.* 59 (1), 114. doi:10.1306/212f8f30-2b24-11d7-8648000102c1865d
- Qing, H. R., and Mountjoy, E. W. (1994). Rare Earth element geochemistry of dolomites in the middle devonian presqu'île barrier, western Canada sedimentary basin: Implications for fluid-rock ratios during dolomitization. *Sedimentology* 41 (4), 787–804. doi:10.1111/j.1365-3091.1994.tb01424.x
- Searl, A. (1989). Saddle dolomite: A new view of its nature and origin. *Mineral. Mag.* 53 (5), 547–555. doi:10.1180/minmag.1989.053.373.05
- Shukla, V., Gregg, J. M., and Sibley, D. F. (1986). Epigenetic dolomitization and the origin of xenotopic dolomite texture; discussion and reply. *J. Sediment. Res.* 56, 733–736. doi:10.1306/212f8a30-2b24-11d7-8648000102c1865d
- Sibley, D. F., Dedoes, R. E., and Bartlett, T. R. (1987). Kinetics of dolomitization. *Geol.* 15 (12), 1112. doi:10.1130/0091-7613(1987)15<1112:kod>2.0.co;2
- Sibley, D. F., and Gregg, J. M. (1987). Classification of dolomite rock textures. *J. Sediment. Res.* 57 (6), 967–975.
- Sibley, D. F. (1991). Secular changes in the amount and texture of dolomite. *Geol.* 19 (2), 151. doi:10.1130/0091-7613(1991)019<0151:scitaa>2.3.co;2
- Sun, W., Chen, M., Wan, Y. L., He, J. L., Lan, Y. F., Wei, H. W., et al. (2020). Closed-system dolomitization process and the significance for petroleum geology, an example from dolostone in the Middle Jurassic Buqu Formation in southern Qiangtang Depression. *Geol. Rev.* 66 (5), 1218–1230. (in Chinese with English abstract).
- Tan, F. W., Wang, J., Wang, X. L., and Du, B. W. (2004). Analysis of carbon and oxygen isotope composition and sedimentary environment of the Yanshipping area of the Qiangtang basin in Middle-Late Jurassic. *Acta Geosci. Sin.* 25 (2), 119–126. (in Chinese with English abstract).
- Tan, F. W., Zhang, R. H., Wang, J., Si, C. S., and Ma, L. Q. (2016). Discussion on basement structures of the late Triassic-early Cretaceous Qiangtang rift basin in Tibet, China. *J. Chengdu Univ. Technol. Sci. Technol. Ed.* 43 (5), 513–521. (in Chinese with English abstract).
- Tian, K. Z., Ji, C. J., Yi, H. S., Tan, M., Jin, F., and Fan, L. S. (2019). Origin of grained dolomite from the Buqu Formation of Zaring area in southern Qiangtang depression. *Geol. China* 46 (2), 398–406. (in Chinese with English abstract).



- Tucker, M. E., and Wright, V. P. (1990). *Carbonate sedimentology*. Oxford: Wiley-Blackwell.
- Vasconcelos, C., and McKenzie, J. A. (1997). Microbial mediation of modern dolomite precipitation and diagenesis under anoxic conditions (Lagoa Vermelha, Rio de Janeiro, Brazil). *J. Sediment. Res.* 67 (3), 378–390.
- Veizer, J., Ala, D., Azmy, K., Bruckschen, P., Buhl, D., Bruhn, F., et al. (1999).  $^{87}\text{Sr}/^{86}\text{Sr}$ ,  $\delta^{13}\text{C}$  and  $\delta^{18}\text{O}$  evolution of Phanerozoic seawater. *Chem. Geol.* 161 (1–3), 59–88. doi:10.1016/s0009-2541(99)00081-9
- Wan, Y. L., Wang, J., Fu, X. G., Tan, F. W., and Wang, Z. W. (2018a). *J. Chengdu Univ. Technol. Sci. Technol. Ed.* 45 (2), 129–141. (in Chinese with English abstract).
- Wan, Y. L., Wang, J., Fu, X. G., and Wang, D. (2020). Geochemical tracing of isotopic fluid of dolomite reservoir in the Middle Jurassic Buqu Formation in southern depression of Qiangtang Basin. *Oil Gas Geol.* 41 (1), 189–200. (in Chinese with English abstract).
- Wan, Y. L., Wang, J., Fu, X. G., and Wang, D. (2018b). Trace element geochemical signatures and significance of rare Earth elements in carbonates in the southern Qiangtang depression. *Sediment. Geol. Tethyan Geol.* 38 (2), 23–35. (in Chinese with English abstract).
- Wan, Y. L., Wang, J., Tan, F. W., Fu, X. G., and Wang, Z. W. (2017a). Dolomite reservoir formation mechanism and pore evolution feature of Buqu formation in the Long'en- Angdaerco area, Qiangtang basin. *J. Northeast Petroleum Univ.* 41 (3), 21–33. (in Chinese with English abstract).
- Wan, Y. L., Wang, J., Wan, F., Fu, X. G., Wang, Z. W., and Shen, L. J. (2017b). Characteristics and indications of rare Earth elements in carbonates in the Buqu Formation, southern Qiangtang Basin. *Petroleum Geol. Exp.* 39 (5), 655–665. (in Chinese with English abstract).
- Wan, Y. L., Zhao, Z., Hu, Z. Z., and Li, X. R. (2021). Controlling factors and their geological significances of order degrees and unit-cell parameters of dolomites in the Middle Jurassic Buqu Formation in Qiangtang Basin. *Sediment. Geol. Tethyan Geol.* 41 (4), 512–523. (in Chinese with English abstract).
- Wang, D., Wang, X., and Chen, D. Z. (2010). Characteristics of saddle dolomite cements in the Cambrian ordovician carbonates in tabei and tazhong area of Tarim Basin. *Chin. J. Geol.* 45 (02), 580–594. (in Chinese with English abstract).
- Wang, J., and Fu, X. G. (2018). Sedimentary evolution of the Qiangtang basin. *Geol. China* 45 (2), 237–259. (in Chinese with English abstract).
- Wang, J., Fu, X. G., Shen, L. J., Tan, F. W., Song, C. Y., and Chen, W. B. (2020). Prospect of the potential of oil and gas resources in Qiangtang basin, xizang (tibet). *Geol. Rev.* 66 (5), 1091–1113. (in Chinese with English abstract).
- Wang, J., Wang, Z. J., Chen, W. X., Fu, X. G., and Chen, M. (2007). New evidences for the age assignment of the NadiKangri Formation in the north Qiangtang Basin, northern tibet, China. *Geol. Bull. China* 26 (4), 404–409.
- Wang, X. T., Zhang, Q. S., Zhang, J., Zhou, S. X., and Li, J. W. (2000). Character study and analysis of dolomite of mesozoic in qingzang plateau. *Acta Sedimentol. Sin.* 18 (4), 555–559. (in Chinese with English abstract).
- Warren, J. (2000). Dolomite: Occurrence, evolution and economically important associations. *Earth-Science Rev.* 52 (1–3), 1–81. doi:10.1016/s0012-8252(00)00022-2
- Whitaker, F. F., and Smart, P. L. (1990). Active circulation of saline ground waters in carbonate platforms: Evidence from the Great Bahama Bank. *Geol.* 18 (3), 200. doi:10.1130/0091-7613(1990)018<0200:acosgw>2.3.co;2
- Wright, W. R. (2001). *Dolomitization, fluid-flow and mineralization of the lower carboniferous rocks of the Irish midlands and dublin basin regions*. Doctoral dissertation, University College Dublin.
- Wu, Z. H., Gao, R., Lu, Z. W., Ye, P. S., Lu, L., and Yin, C. Y. (2014). Structures of the Qiangtang basin and its significance to oil- gas exploration. *Acta Geol. Sin.* 88 (6), 1130–1144. (in Chinese with English abstract).
- Wu, Z. H., Liu, Z. W., Zhao, Z., Ji, C. J., and Ye, P. S. (2016). Thrust and uplift of the lung'en-angdarco paleo-oil reservoirs in the Qiangtang basin. *Acta Geol. Sin.* 90 (4), 615–627. (in Chinese with English abstract).
- Xiong, Y., Tan, X. C., Zhong, S. K., Xiao, D., Wang, B. B., Yang, M. Y., et al. (2022). Dynamic paleokarst geochemistry within 130 Myr in the middle ordovician shanganning carbonate platform, north China. *Palaeogeogr. Palaeoclimatol. Palaeoecol.* 591, 110879. doi:10.1016/j.palaeo.2022.110879
- Xiong, Y., Wang, L. C., Tan, X. C., Liu, Y., Liu, M. J., Qiao, Z. F., et al. (2021). Dolomitization of the ordovician subsalt majiagou Formation in the central ordos basin, China: Fluid origins and dolomites evolution. *Pet. Sci.* 18 (2), 362–379. doi:10.1007/s12182-020-00522-1
- Yang, R. H., Li, C., Yang, D. M., He, Z. H., Ren, Y. S., and Liu, J. (2000). Mesozoic tectonic-petrographic evolution and oil- gas perspective in Qiangtang basin, tibet. *J. Changchun Univ. Sci. Technol.* 30 (3), 237–242. (in Chinese with English abstract).
- Yang, W., Liu, M. C., Wei, G. Q., Jin, H., Xie, W. R., Wu, S. J., et al. (2021). Lithofacies paleogeography and characteristics of large-scale reservoirs of the middle triassic leikoupo Formation in Sichuan Basin, China. *J. Nat. Gas Geoscience* 6 (5), 255–268. doi:10.1016/j.jnggs.2021.09.002
- Yang, Y., Xie, J. R., Zhao, L. Z., Huang, P. H., Zhang, X. H., Chen, C., et al. (2021). Breakthrough of natural gas exploration in the beach facies porous dolomite reservoir of middle permian maokou Formation in the Sichuan Basin and its implications: A case study of the tridimensional exploration of well JT1 in the central-northern Sichuan Basin. *Nat. Gas. Ind. B* 8 (4), 393–401. doi:10.1016/j.ngib.2021.07.010
- Yi, H. S., Chen, Z. Y., Ji, C. J., Yang, X. P., Xiong, G. Q., and Wu, C. H. (2014). New evidence for deep burial origin of sucrosic dolomites from Middle Jurassic Buqu Formation in southern Qiangtang basin. *Acta Petrol. Sin.* 30 (3), 737–746. (in Chinese with English abstract).
- Yi, H. S., Gao, C. W., Zhang, X. Q., and Li, J. H. (2004). Microscopic diagenetic fabrics of dolomite reservoir from Shuanghu paleo-oil pool of Qiangtang basin and its petroleum exploration implications. *J. Chengdu Univ. Technol. Sci. Technol. Ed.* 31 (6), 611–615. (in Chinese with English abstract).
- Yi, H. S., and Xia, G. Q. (2022). Stratigraphic position of higher quality source rocks and distribution of oil-bearing dolomites in the Qiangtang Basin. *Sediment. Geol. Tethyan Geol.* (in Chinese with English abstract). doi:10.19826/j.cnki.1009-3850.2022.04005
- Yu, Z., Zhou, J. G., Ding, Z. C., Wei, L. B., Wei, Y., Wu, X. N., et al. (2020). Reservoir characteristics and Genesis of the Ordovician  $\text{M}_5^{4+1a}$  in the central and eastern parts of the Ordos Basin, China. *J. Nat. Gas Geoscience* 5 (5), 285–297. doi:10.1016/j.jnggs.2020.09.001
- Yue, H., Liu, F., Zhang, H. L., Zhou, C. L., Chen, W. H., Xiao, Z. H., et al. (2021). Specified staged acid fracturing of horizontal well for strong-heterogeneity carbonate gas reservoirs: A case study on the gas reservoir of the fourth member of upper sinian dengying Formation in gaoshiti-moxi area of the central Sichuan Basin. *Nat. Gas. Ind. B* 8 (5), 484–493. doi:10.1016/j.ngib.2021.08.010
- Zhang, L. Q., Ji, Y. L., and Li, Y. T. (2001). Reservoir characteristics of the jurassic dolomite in the Qiangtang basin. *Petroleum Geol. Exp.* 23 (4), 384–389. (in Chinese with English abstract).
- Zhang, X. Q., Yi, H. S., and Zhu, Y. T. (2005). Study on reservoir characteristics of the dolomite in the Shuanghu area, Qiangtang basin. *J. Southwest Petroleum Univ. Sci. Technol. Ed.* 27 (5), 10–13. (in Chinese with English abstract).
- Zhang, Y. X., Li, Y., Zhang, K. J., and Li, Y. L. (2006). Characteristics of mid-upper jurassic carbonate rocks in the yichangma area, Qiangtang basin, tibet: Implications for the sedimentary environment. *Geol. China* 33 (2), 393–400. (in Chinese with English abstract).
- Zhao, W. Z., Wang, Z. C., Jiang, H., Fu, X. D., Xie, W. R., Xu, A. N., et al. (2020). Exploration status of the deep Sinian strata in the Sichuan Basin: Formation conditions of old giant carbonate oil/gas fields. *Nat. Gas. Ind. B* 7 (5), 462–472. doi:10.1016/j.ngib.2020.09.004
- Zhao, Z., Wu, Z. H., Yang, Z. Y., and Ji, C. J. (2020). Establishing the chronostratigraphic framework of the continental red beds in Central Qiangtang Basin: Constrained by zircon U-Pb ages. *Geol. Rev.* 66 (5), 1155–1171. (in Chinese with English abstract).
- Zhu, J. Q., and Li, Y. T. (2000). Types, origin and reservoir characteristics of the jurassic dolostones in the Qiangtang basin, north tibet. *J. Palaeogeogr.* 2 (4), 30–42. (in Chinese with English abstract).